SANDIA REPORT

SAND2015-11072
Unlimited Release
Printed December 2015

Final Technical Report: Distributed Controls for High Penetrations of Renewables

Raymond H. Byrne, Jason C. Neely, Lee J. Rashkin, Dakota Roberson, Daniel J. Trudnowski, and David G. Wilson

Prepared by
Sandia National Laboratories
Albuquerque, New Mexico 87185 and Livermore, California 94550

Sandia National Laboratories is a multi-program laboratory managed and operated by Sandia Corporation, a wholly owned subsidiary of Lockheed Martin Corporation, for the U.S. Department of Energy's National Nuclear Security Administration under contract DE-AC04-94AL85000.

Issued by Sandia National Laboratories, operated for the United States Department of Energy by Sandia Corporation.

Available to DOE and DOE contractors from
U.S. Department of Energy
Office of Scientific and Technical Information
P.O. Box 62
Oak Ridge, TN 37831

Telephone: (865) 576-8401
Facsimile: (865) 576-5728
E-Mail: reports@adonis.osti.gov
Online ordering: http://www.osti.gov/bridge

Available to the public from
U.S. Department of Commerce
National Technical Information Service
5285 Port Royal Rd
Springfield, VA 22161

Telephone: (800) 553-6847
Facsimile: (703) 605-6900
E-Mail: orders@ntis.fedworld.gov
Online ordering: http://www.ntis.gov/help/ordermethods.asp?loc=7-4-0#online

SAND2015-11072
Unlimited Release
Printed December 2015

Final Technical Report: Distributed Controls for High Penetrations of Renewables

Raymond H. Byrne, Jason C. Neely, Lee J. Rashkin, Dakota Roberson, and David G. Wilson
Sandia National Laboratories
Data Analysis and Exploitation Department
Albuquerque, NM 87185-0576
email: rhbyrne@sandia.gov

Daniel J. Trudnowksi
Electrical Engineering Department
Montana Tech University
1300 W. Park Street
Butte, MT 59701

Abstract

The goal of this effort was to apply four potential control analysis/design approaches to the design of distributed grid control systems to address the impact of latency and communications uncertainty with high penetrations of photovoltaic (PV) generation. The four techniques considered were: optimal fixed structure control; Nyquist stability criterion; vector Lyapunov analysis; and Hamiltonian design methods. A reduced order model of the Western Electricity Coordinating Council (WECC) developed for the Matlab Power Systems Toolbox (PST) was employed for the study, as well as representative smaller systems (e.g., a two-area, three-area, and four-area power system). Excellent results were obtained with the optimal fixed structure approach, and the methodology we developed was published in a journal article. This approach is promising because it offers a method for designing optimal control systems with the feedback signals available from Phasor Measurement Unit (PMU) data as opposed to full state feedback or the design of an observer. The Nyquist approach inherently handles time delay and incorporates performance guarantees (e.g., gain and phase margin). We developed a technique that works for moderate sized systems, but the approach does not scale well to extremely large system because of computational complexity. The vector Lyapunov approach was applied to a two area model to demonstrate the utility for modeling communications uncertainty. Application to large power systems requires a method to automatically expand/contract the state space and partition the system so that communications uncertainty can be considered. The Hamiltonian Surface Shaping and Power Flow Control (HSSPFC) design methodology was selected to investigate grid systems for energy storage requirements to support high penetration of variable or stochastic generation (such as wind and PV) and loads. This method was applied to several small system models.

keywords: distributed control, renewable generation.

This page intentionally blank.

Final Technical Report

Project Title:	Distributed Controls for High Penetrations of Renewables (e.g. 100% of peak load)
Project Period:	10/1/14-9/30/15
Budget Period:	10/1/14-9/30/15
Reporting Period:	10/1/14-9/30/15
Reporting Frequency:	Quarterly
Submission Date:	11/14/15
Recipient: **Address:**	Sandia National Laboratories 1515 Eubank SE Albuquerque, NM 87123
Website:	www.sandia.gov
Award Number:	Agreement No. 29094
Project Team:	Sandia National Laboratories Montana Tech University
Principal Investigator:	Ray Byrne, Ph.D. Phone: (505) 844-8716 Email: rhbyrne@sandia.gov
Business Contact:	Shannon Boynton Phone: (505) 284-2631 Email: sboynto@sandia.gov
HQ Tech Manager:	Guohui Yuan, Ph.D.
HQ Project Officer:	Christine Bing
HQ Financial Officer:	Jacob Mees

Executive Summary

keywords: transient stability, small signal stability, renewable energy, power system stability.

The goal of this effort was to apply four potential control analysis/design approaches to the design of distributed grid control systems to address the impact of latency and communications uncertainty with high penetrations of photovoltaic (PV) generation. This research was funded by the DOE SunShot program, with the goal of enabling 100s of Gigawatts (GW) of solar generation. This project was executed over a 10-month period in FY15. The four techniques considered were: optimal fixed structure control; Nyquist stability criterion; vector Lyapunov analysis; and Hamiltonian design methods. The goal was to apply these approaches to a large scale system and a represntative small system. A reduced order model of the Western Electricity Coordinating Council (WECC) developed for the Matlab Power Systems Toolbox (PST) was employed for the study, as well as representative smaller systems (e.g., a two-area, three-area, and four-area power system). Excellent results were obtained with the optimal fixed structure approach, and the methodology we developed was published in a journal article. This approach is promising because it offers a method for designing optimal control systems with the feedback signals available from Phasor Measurement Unit (PMU) data as opposed to full state feedback or the design of an observer. The Nyquist approach inherently handles time delay and incorporates performance guarantees (e.g., gain and phase margin). We developed a technique that works for moderate sized systems, but the approach does not scale well to extremely large system because of computational complexity.

For the vector Lyapunov approach, we investigated several test cases for a two-area system model. This approach is promising, but additional research is required to overcome an obstacle: automatic partitioning of the state space and expansion/contraction of the state space to remove the uncertainty associated with interconnection impedances (the partitioning problem has been solved, it needs to be addressed in conjunction with the expansion/contraction). The Hamiltonian Surface Shaping and Power Flow Control (HSSPFC) design methodology was selected to investigate grid systems for energy storage requirements to support high penetration of variable or stochastic generation (such as wind and PV) and loads. Specially designed models that are based on the physical (kinetic and potential) energy of the system (the Hamiltonian) allow for the identification of static stability criterion. The Hamiltonian rate (or power flow) determines the dynamic stability criterion. This leads directly to the stability and performance based on energy storage; power, energy and frequency requirements needed to be realized. The technique allows for the inclusion of nonlinear control law formulations. Several examples were investigated for a one machine infinite bus (OMIB) and a four generator Kundur like model. Further developments will need to be explored to expand the technique specific for PV inverter systems operating in coordination with spinning machines.

As part of the preliminary efforts, we updated the minni-WECC model to include PV generation, added PV models to the PST Toolbox, and added linearization code for the PV plants. The original goal was to achieve almost 100% PV generation. We were able to reach 75% without any additional controls, and 93% with minimal controls (e.g., frequency droop and voltage support). With additional tweaking, we were able to reach 95%. Based on the difficulty with reaching 100% renewable penetration with the PST model, and previous research with General Electric's Positive Sequence Load Flow (PSLF) software models, additional research is required to develop meaningful grid models with very high renewable generation levels. The eigenvalue and transient stability results for the minni-WECC with high PV penetrations were consistent with previous research. As PV penetration increases, system inertia decreases and mode frequencies increase, with minimal impact on mode damping. Similarly, the reduction in system inertia increases the speed of the drop in frequency as a result of a loss of generation (e.g., a Palo Verde Trip of 1.4 GW). The frequency nadir also decreases with increased PV generation. It should be noted that the minni-WECC

model is a reduced-order model developed primarily for modal analysis of inter-area oscillations in the western North American power grid. The fact that we were able to reach 75% solar penetration with no additional controls should not be interpreted as the main result - there will be difficulties in achieving this penetration that were not accurately captured by the reduced order model. Rather, the main takeaway should be that displacing traditional generation inertia with PV will result in higher mode frequencies, with similar damping in most cases. Also, the frequency nadir after a generator drop will decrease with increasing PV generation and no additional controls for the PV. Including frequency droop control on the PV can mitigate this effect.

The PST and minni-WECC model are open source code, and the models and algorithms developed under this effort will be made publicly available on the "PV_LIB" web site (https://pvpmc.sandia.gov/). The mathematical techniques summarized in this report are intended to provide tools for the design and analysis of power system control systems with time delay that is naturally associated with distributed control and communications.

Contents

Abstract 3

Executive Summary 6

Table of Contents 8

1 Background 9

2 Project Objectives 16

3 Project Results and Discussion 16
- 3.1 System Model . . . 16
- 3.2 Linear Minni-WECC Model with Droop and Voltage Gain Control . . . 18
- 3.3 Small Signal and Transient Analysis with Minimal Controls . . . 20
- 3.4 Fixed Structure Optimal Control . . . 24
  - 3.4.1 Minni-WECC Scenario: Damping the East-West Mode . . . 26
  - 3.4.2 Phase Margin in Multi-Mode Systems . . . 32
- 3.5 Nyquist Stability Methods . . . 34
  - 3.5.1 Three-Area Model . . . 34
  - 3.5.2 Minni-WECC Nominal Case . . . 40
- 3.6 Vector Lyapunov Methods . . . 43
  - 3.6.1 Two-Area System . . . 44
- 3.7 Hamiltonian Surface shaping and Power Flow Control (HSSPFC) . . . 49
  - 3.7.1 Example 1: OMIB model and control . . . 49
  - 3.7.2 UPFC Control Simulation . . . 50
  - 3.7.3 Simple AC Inverter Electric Grid Systems . . . 54
  - 3.7.4 Example 2: Kundur "like" Model . . . 56

4 Significant Accomplishments and Conclusions 59

5 Inventions, Patents, Publications, and Other Results 61

6 Path Forward 61

Acknowledgement 62

References 63

1 Background

Small system stability refers to the response of a system to small disturbances. Because the disturbances are small, the system response can be modeled with a linearization of the system about the current operating point. Typically, a linear time invariant state space model of the form:

$$\dot{x}(t) = Ax(t) + Bu(t) \tag{1}$$

$$y(t) = Cx(t) + Du(t) \tag{2}$$

is employed for small signal analysis. The system dynamics are fully described by the constant matrices (A, B, C, D). The state of the system at time t is captured by the vector $x(t)$. The input to the system is modeled by $u(t)$ while the output of the system is $y(t)$. For the physical system, all of the states are typically not directly observable. However, for simulation and analysis purpose, the C matrix is usually the identity matrix (all states are observable). For physical systems, the D matrix is normally 0 unless there is some sort of feed-forward term in the model (e.g., the output moves instantaneously when an input changes). For power systems, small perturbations consist of variations in load or generation, as well as small disturbances caused by faults. Transient stability is concerned with the response of the system to large disturbances, like a generator trip, where the response of the system often includes nonlinearities.

Small system stability is a concern in power systems because outages in the past have been partially attributed to small signal instability [1]. All large power systems have low frequency oscillations in system frequency where large generation and load complexes slowly oscillate against each other. These oscillations are typically under 1 Hz. They are commonly referred to as inter-area oscillations, and they are so prevalent that they are often named. For example, several of the known oscillations in the western interconnection in the United States (U.S.) are listed below. The 1996 West coast blackout was partially attributed to

Table 1: Known inter-area oscillation modes in the western North American power grid [2].

Mode Name	**Nominal Frequency (Hz)**
North-South A mode	0.25 Hz
North-South B mode	0.40 Hz
East-West mode	0.50 Hz
British Columbia mode	0.60 Hz
East-West southern mode	0.70 Hz
Montana mode	0.80 Hz

unstable oscillation of the North-South A mode. This is illustrated in Figure 1, which shows the power flow on the California-Oregon Intertie (COI) in the minutes preceding the system breakup. The COI is an AC transmission line that connects the pacific northwest to southern California. Lightly damped 0.25 Hz oscillations are present several minutes before the undamped oscillations which ultimately resulted in a system breakup. A review of inter-area electromechanical oscillations found in the Continental Europe power system is found in [3]. The impact of increased levels of renewable generation on the transient stability of the western U.S. power grid were identified in the Western Wind and Solar Integration Study (WWSIS) [4, 5]. They concluded that except for the most extreme cases, traditional mitigation methods could accommodate the increased wind and solar generation. The extreme case approached 55% renewable generation for brief periods over the course of a year's dispatch.

Because inter-area oscillations can impact reliability in any large power system, their mitigation is an active area of study. Schemes for damping these oscillations include: real power modulation of high

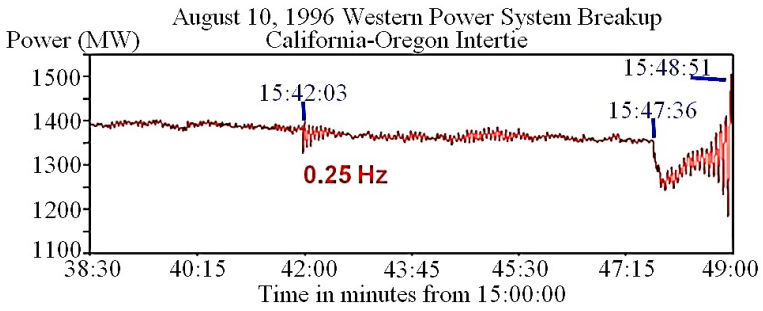

Figure 1: The power flow on the COI during the August 10^{th}, 1996 Western power system breakup.

voltage DC links [2]; real power modulation of energy storage [6, 7]; power modulation of wind generation [8]; voltage modulation with Static Var Compensators (SVC) [9]; and thyristor controlled series compensator (TCSC) modulation [10]. With evolving grid dynamics as the quantity of renewable generation has increased and will only increase further in the future, there is additional concern on the impacts of high renewable penetrations on the small signal stability of power grids. A preliminary study described in [11] came to the following conclusions:

- increasing renewable generation and the accompanying decrease in system inertia will increase the frequency of inter-area modes.
- for the WECC model, mode damping stayed roughly constant with increasing renewable generation with the exception of an East-West mode where the damping decreased.

This results is captured in Figure 2, which shows the increase in mode frequency of the WECC North-South B mode as renewable generation is increased.

As the amount of renewable generation increases, distributed control algorithms will likely be required to maintain or improve grid performance and reliability. Inherent to all distributed control schemes is the negative impact of communications latency and the loss of data links. Communications latency is modeled as

$$\text{time delay } = e^{-s\tau} \tag{3}$$

where s is the complex variable $s = j\omega + \sigma$ and τ is the time delay in seconds. The reduction in phase margin is directly proportional to the time delay τ. As the time delay increases, the phase margin is decreased until the system becomes unstable. Similarly, the loss of a feedback signal can also lead to instability. Therefore, the goal of this effort was to apply and assess four different control approaches that are well suited for modeling communications delay and designing control systems that are robust with respect to the loss of communications. The four approaches considered are:

1. Vector Lyapunov analysis
2. Fixed-structure Optimal Control
3. Nyquist Stability Analysis
4. Hamiltonian Control Design

Vector Lyapunov Analysis

Vector Lyapunov analysis is used to determine the impact of communications connectivity on control system stability. Vector Lyapunov analysis is a powerful tool for quantifying the stability regions of large

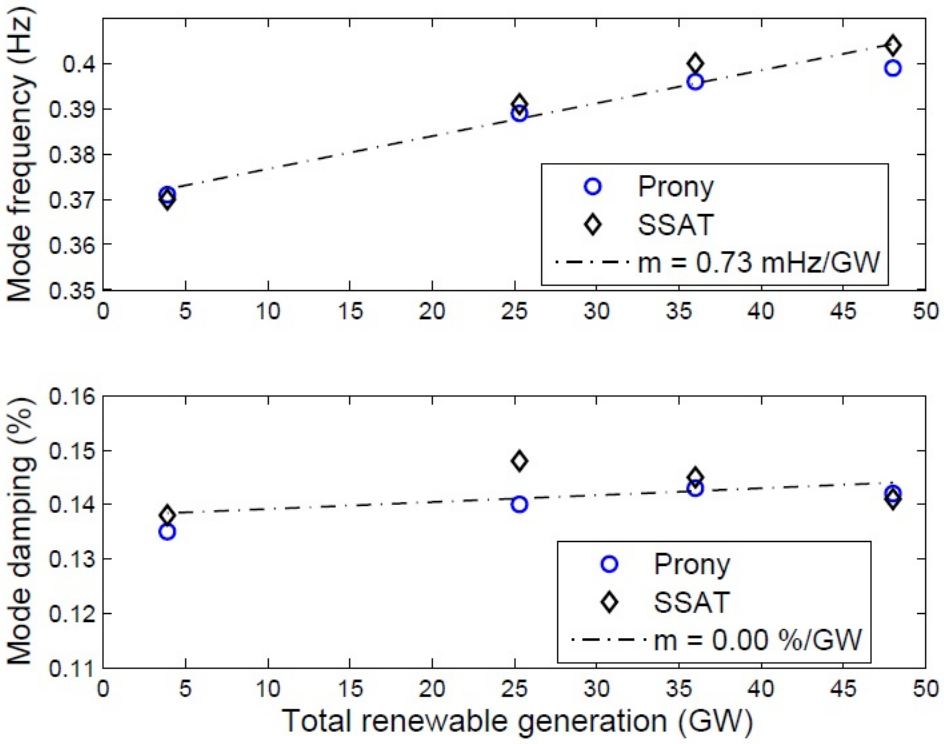

Figure 2: WECC North-South B mode frequency and damping as a function of renewable generation [11].

distributed control systems. This approach has been successfully applied in the past by project team members to analyze the performance of distributed control algorithms for mobile robots [12]. This theory has been applied to small power system networks as well, but it has not been scaled to larger grids. Assuming that a control function has already been identified, the closed loop dynamics of the discrete-time system can be written as

$$S: \; x_i(k+1) = g_i(k, x_i) + \tilde{g}(k, \bar{x}) \tag{4}$$

where $\bar{x}$ is the state of S at time t. x_i is the state of the i^{th} subsystem at time k. The function g_i describes the local dynamics of S_i and $\tilde{g}_i$ represents the dynamic interaction of S_i with the rest of the system. An interconnection matrix, $\bar{E} = (\bar{e}_{ij})$ is used to describe the communications connectivity between components of the distributed system. Structural perturbations of the system are introduced by assuming the elements of the interconnection matrix that are '1' can be replaced by any number between 0 and 1 (to represent the strength of coupling between individual subsystems).

A system is connectively stable if it is stable in the sense of Lyapunov for all possible $E = (e_{ij})$ [13]. This is very powerful because it proves that a system will be stable even if a communications link is lost. For a distributed grid control system with high penetration of solar, this approach can be used to define stability regions in the face of communications failures, as well as a region of stable controller gains. An example from the robotics application is shown in Figure 3.

Vector Lyapunov techniques have also been applied to power systems. An application to transient stability applied to an $m-$machine system is described in [14]. However, to arrive at an analytic solution the following assumptions had to be made:

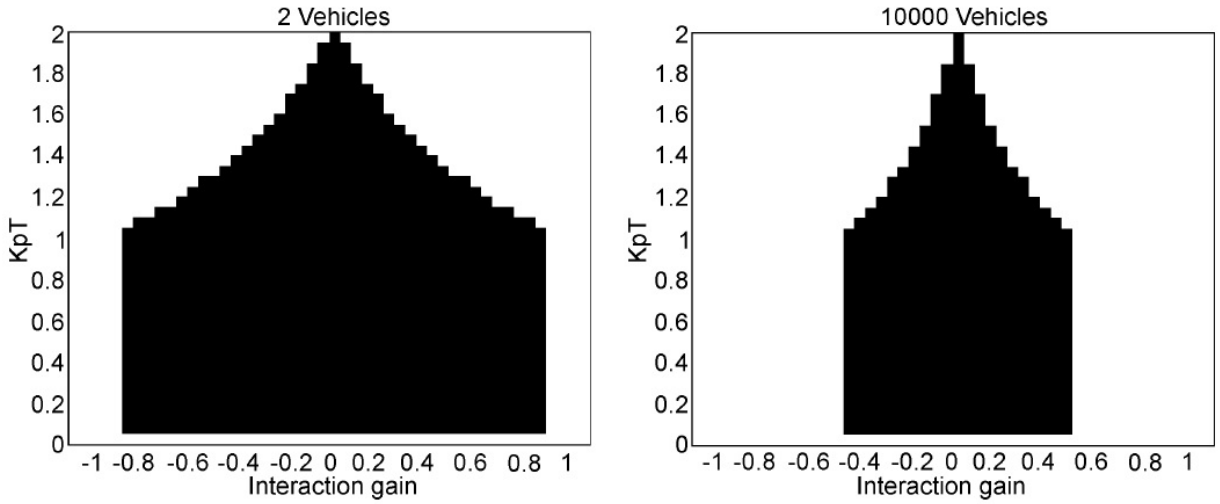

Figure 3: Distributed control of multiple robots. Stability region for N=2 (left) and N=1000 (right) vehicle case. The interaction gain is the feedback gain across communication links to other nodes [12].

- inertia, electrical power, and voltage are constant for all machines
- uniform damping for each subsystem

A direct application of Lyapunov techniques applied to the transient stability problem is presented in [15]. Analytic solutions were derived for a single-machine system and a two-machine system with uniform damping. Higher order systems were too difficult because of the transfer conductances. A method for automatically decomposing large power systems into smaller subsystems is described in [16]. A parallel implementation of the epsilon decomposition was derived for large sparse systems. The epsilon decomposition performs the following operation: on given a matrix $A = [a_{ij}]$ and a value of parameter $\epsilon > 0$, all elements satisfying $|a_{ij}| \leq 0$ are set to zero. The resulting sparsified matrix is then permuted into a block diagonal form. All the variables in the same block are considered to be strongly coupled. This is equivalent to the following decomposition:

$$A = A_D + \epsilon A_C \tag{5}$$

where A_D is a block diagonal matrix and the magnitude of the elements of A_C are less than or equal to one.

Optimal Fixed Structure Control

Optimal fixed structure control is used to identify optimal distributed control solutions. A fixed structure control system is defined as a control system where the structure of the control algorithm is identified first (e.g. frequency feedback), and then the controller gains are identified. Typically, a multi-input multi-output (MIMO) optimal control system design attempts to minimize a cost function

$$J = \int_0^T (x^T Q x + u^T R u) dt \tag{6}$$

where x is the state vector and u is the input vector. The R matrix represents the penalty on the input while the Q matrix represents the penalty on the state. The solution to the LQR (Linear Quadratic Regulator) problem requires full state feedback (e.g., access to all the states). For a scenario with limited

state feedback (e.g., only use frequency at each control node) or a predefined feedback architecture (e.g., regional communications), one option is to design an optimal fixed structure controller [17]. We extended this design methodology and applied it towards distributed controller design for a linearized power system model. Traditional Linear Quadratic Regulator (LQR) control designs are very robust, with an infinite gain margin and 60 degree phase margin. Although it was not the focus of this effort, we feel that some robustness properties may be guaranteed for optimal fixed structure control.

Nyquist Stability Criterion

For representative reduced order models, the Nyquist stability criterion can be applied to identify the tradeoffs between control system performance (e.g. gain and phase margin) and communications latency. For transfer function models, the Nyquist stability criterion is a powerful tool for evaluating the control system performance with communications delays [18]. This approach can also be applied numerically when input/output data is available in lieu of model (e.g. PSLF simulations) for large systems. It is also possible to apply this approach to multi-input multi-output (MIMO) systems using the generalized Nyquist criterion for transfer function matrix representations; specifically, the relationship between time delay, stability bounds, and control system performance (e.g., gain and phase margins) can be captured.

The project team has applied the Nyquist stability criteria to analyze the performance of energy storage systems in damping inter-area oscillations [6]. Once a system model has been developed (single-input single-output), the first step is to define minimum performance requirements in terms of gain and phase margin. This can be represented graphically as shown in Figure 4 (left). Then, either using the model or input-output data, one can calculate acceptable gain values for the controller as a function of communications latency, as shown in Figure 4 (right).

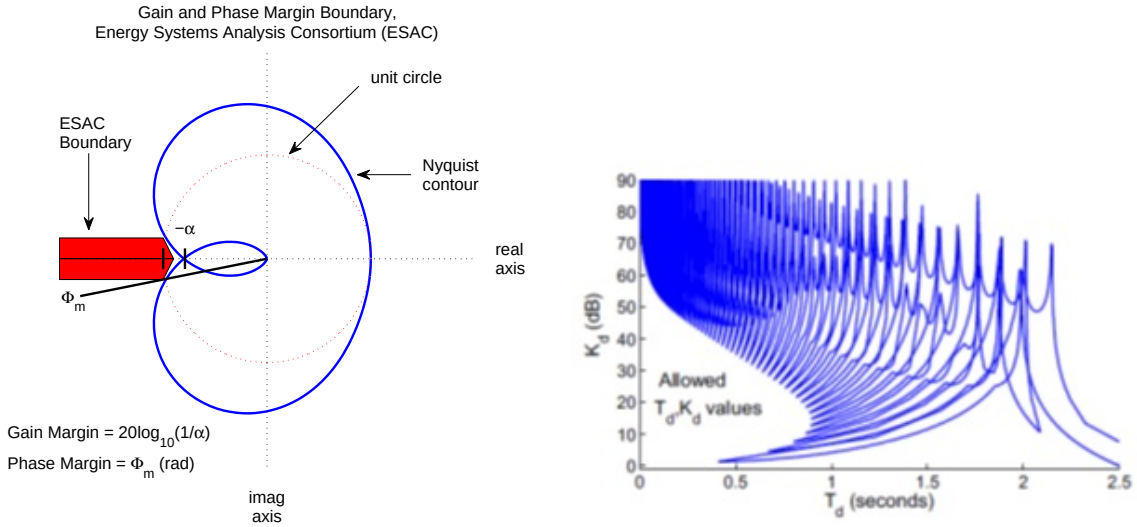

Figure 4: ESAC (Energy System Analysis Consortium) boundary for a specified gain and phase margin (left), allowed controller gains as a function of communication latency (right) [6].

A similar process can be used to analyze distributed control systems for high penetrations of solar. This is especially useful for looking at the tradeoffs between communications latency and control system performance. Smaller latencies usually correspond to closer spatial separation and/or higher performance communication links. This impacts control system architecture (e.g. local vs. global communications) as well as communications requirements.

Hamiltonian Optimal Control

The fourth methodology is Hamiltonian based optimal control [19]. The Hamiltonian, H, represents the sum of the kinetic and potential energy of the system.

$$H = \text{kinetic energy} + \text{potential energy} \tag{7}$$

In order for a system to be stable, the derivative of the Hamiltonian must be less than 0 (e.g., decreasing energy). For previous micro-grid research, the team members have assumed a fixed controller structure (e.g. a proportional-integral controller) at each node, and derived regions of acceptable gains based on the constraint on the derivative of the Hamiltonian. A recent publication by the team has explored the tradeoffs between communications update rate and the control effort required (an energy storage device in this example) to stabilize a D.C. micro-grid with 100% renewable generation. The cost function was defined as the variance of the power output of the energy storage system.

Below is a summary of each control system methodology. Each methodology can be applied to frequency and voltage droop, as well as other more complex control algorithms.

Vector Lyapunov Stability

• This is a stability test that guarantees connective stability in the face of structured perturbations. The structured perturbations may be used to model plant uncertainty and/or communications uncertainty.

• Given a control system structure, this technique may be applied to estimate regions of stability as control gains are varied.

• While this approach handles robustness with respect to communication drop outs, latency must be incorporated via a an approximation (e.g., Pade approximation).

• This approach requires a state space system model. For large systems, the model must be automatically partitioned into smaller subsystems. Overlapping states require an expansion/contraction of the state space model. The approach also extends well to nonlinear systems.

Optimal Fixed Structure Control

• Allows for optimal control system design with feedback from a subset of selected states. This is well suited for PMU-based control systems where data is only available where PMUs are present.

• While no robustness properties have been derived, we feel that further analysis might yield some degree of robustness with respect to gain and phase margin (beyond the scope of this effort). The phase margin robustness properties are well suited for systems with time delay.

• This technique is a control system synthesis tool that requires a state space system model.

Nyquist stability

• The Nyquist stability criterion is an excellent tool for assessing stability of systems with communications delay. It is also possible to include minimum performance bounds expressed as a gain/phase margin.

• This technique can be applied to analytical models as well as test data from an operational system (e.g., magnitude and phase as the frequency is swept).

Hamiltonian Design Techniques

• Explicit analytical formulation of the total energy (Hamiltonian) in the system (kinetic and potential energy) leads to specific static stability criteria. For electric grid systems this is typically the energy storage (physical; inertial, capacitance, inductance, chemical, or information flow, etc.). This defines the grid stability, or G-L = delta ES.

• The Hamiltonian rate or power flow leads to specific dynamic stability criteria. By incorporating feedback control for the energy storage systems, the dynamic transient response can be determined with respect to the renewable energy generation inputs and grid load demands. This defines the grid performance.

• Nonlinear control laws can be easily incorporated into the formulation to help design specific performance margins into both the static and dynamic stability criteria.

• This design technique is typically applied to the full nonlinear system and does not require linearization of the system.

• Information flow (communication through feedback control) can be incorporated as additional kinetic or potential functions such that information flow versus physical energy storage can be evaluated which ultimately leads to determining the peak power, energy and frequency response requirements/ specifications for the energy storage systems.

Recent efforts have proposed model predictive control (MPC) for the distributed control of solar generation. Examples are found in [20, 21, 22]. In [20], the authors address a limitation of model predictive control, that requires an accurate system model, by employing a data-driven subspace approach which only requires the input and output measurements to model the subsystems of the distributed system. In

[21], a model predictive control optimization is proposed for the control of wind and solar with integrated energy storage in a direct current (DC) grid. Model predictive control applied to an AC power system with wind, solar, and energy storage is described in [22]. Model predictive control was initially developed and applied to the petrochemical industry in the 1970's [23]. Current applications include the chemical and microelectronic industries [23]. One of the benefits of MPC is that it is formulated as an optimization problem, which can be applied to the optimal dispatch of a power system. However, in order to incorporate time delays in MPC, Lyapunov methods are often employed [24].

The next section discusses the project objectives.

2 Project Objectives

The goal of this research was to develop several distributed control algorithms that not only preserve, but enhance the performance and reliability of the power system with respect to frequency regulation and electromechanical stability. This knowledge and understanding is critical for meeting the Sunshot goals of "achieving high penetration of solar generation at both the transmission and distribution levels in a cost-effective manner, while ensuring safety and reliability of the grid". Developing control algorithms that mimic conventional generation will likely never result in performance better than the current grid. This research is also well-aligned with the Sunshot long-term goals of enablement of wider deployment and reduction in costs.

Since there is a strong relationship between the distributed control system design and communications requirements, we purposely selected four different control approaches that work well with handling time delay and communications uncertainty. The four control approaches considered were:

1. Vector Lyapunov analysis
2. Fixed-structure Optimal Control
3. Nyquist Stability Analysis
4. Hamiltonian Control Design

The intent was to apply each technique to a large and small power system model. The minni-WECC was representative of a large power system, while a two-area, three-area, and four-area systems were employed as surrogates for small power systems. The primary measure of performance was the eigenvalues of the linearized system model. Transient simulations were performed where applicable to ensure that transient stability was not negatively impacted by any control scheme. The goal was to analyze systems with very close to 100% PV generation, e.g., 99.9%.

The next section summarizes the results from the project.

3 Project Results and Discussion

3.1 System Model

All analysis for this project was performed in MATLAB using the Power System Toolbox (PST). The PST was originally developed by Prof. Joe Chow and Dr. Kwok Cheung in the early 1990's [25]. It was further marketed and developed by Graham Rogers, and is currently available from Dr. Luigi Vanfretti's web site [26]. The "minni-WECC" model, developed by Montana Tech, and employed by Sandia for the last few years, was used as a surrogate for the WECC [2]. The current full WECC model has approximately 19,000

buses, 4,000 generators, 9,000 loads, 8,000 transformers, and 16,000 transmission lines. The structure of the reduced order minni-WECC model is shown in Figure 6. The reduced order minni-WECC model contains approximately 122 buses, 172 transmission lines, 35 generators, and 66 loads. The minni-WECC has been primarily used for modal analysis of inter-area oscillations, and the development of mitigation schemes. The modes of the minni-WECC have been correlated with observed PMU data for many types of system disturbances [2].

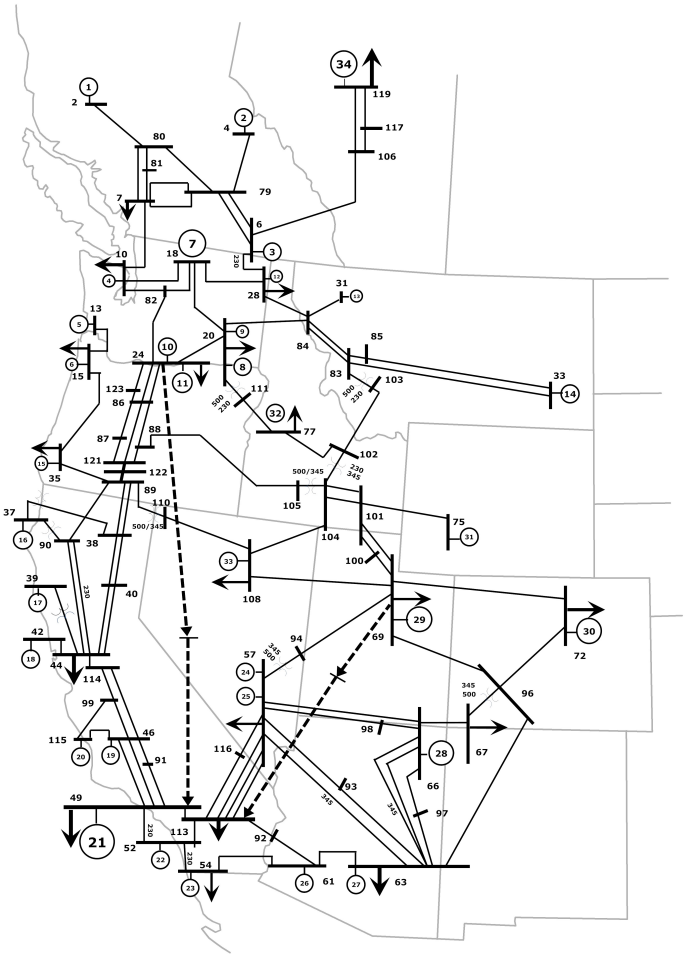

Figure 5: "minni-WECC" reduced order model for the MATLAB Power Systems Toolbox [7].

In order to add solar generation to the model, solar plants were co-located with all generators, and a scale factor α was used to scale the amount of traditional generation relative to PV generation. When $\alpha = 0$, the model contains no PV generation. When $\alpha = 1$, the model contains 100% PV generation. By scaling the generator base MVA, the 'size' and thus inertia of the traditional generation is scaled properly as the penetration of PV increases. The nominal real and reactive generation is given by P_0 and Q_0. The

real and reactive control effort at the PV plant are P_C and Q_C.

$$Pgen = (1-\alpha)P_0 \quad (8)$$
$$Qgen = (1-\alpha)Q_0 \quad (9)$$
$$Psolar = \alpha P_0 + P_C \quad (10)$$
$$Qsolar = \alpha Q_0 + Q_C \quad (11)$$
$$\text{base MVA (with solar generation)} = (1-\alpha)(\text{base MVA}) \quad (12)$$

The advantage of this approach is that power flows remain roughly the same for all cases. Any changes can be directly attributed to the PV displacement of traditional generation, so this provides a favorable framework for investigating the impact of high PV penetrations. A disadvantage is that in reality, increased PV penetrations will likely be in areas favorable to PV. Going down this path would have required the development of a new WECC model, which would have been a significant investment, and inappropriate for a 1-year project. This is especially true when considering PV penetrations approaching 100% of load. Likewise, considering behind the meter versus utility solar is beyond the scope of this effort. This level of modeling detail is not captured in a lumped parameter model like the minni-WECC.

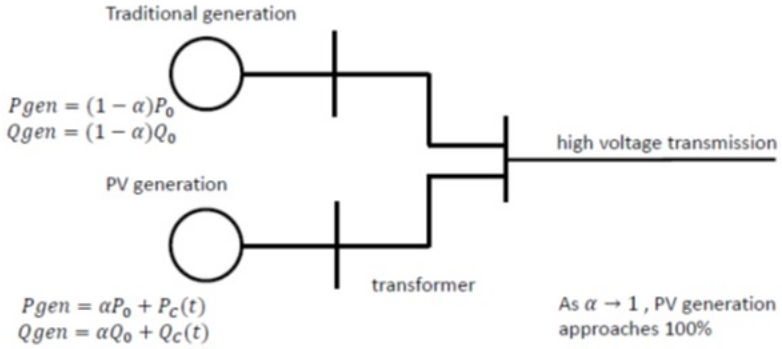

Figure 6: MinniWECC modification to accommodate high PV penetrations.

After adjusting the minni-WECC to accommodate high PV penetrations, models had to be developed for PV generation. Two different models were developed: power injection and current injection. Finally, the PST linearization code had to be updated to include the PV generation. The next section describes the derivation of the linear model of the PV plants.

3.2 Linear Minni-WECC Model with Droop and Voltage Gain Control

This section reviews the derivation of the linearized PV models that incorporate frequency droop and voltage support. Given the following state space model

$$\dot{x_1} = Ax_1 + B_1\Delta P + B_2\Delta Q \quad (13)$$

where the i^{th} entry of $\Delta P_i = (P_i - P_0)$ and the i^{th} entry of $\Delta Q_i = (Q_i - Q_0)$,

$$\Delta\theta = C_1 x_1 \quad (14)$$

where $\Delta\theta$ is the vector of voltage angle deviations at each of the individual injection buses, and

$$\Delta V = C_2 x_1 \tag{15}$$

where ΔV is the vector of voltage magnitude deviations at each of the individual injection buses, we can develop a control scheme using real and reactive power actuation at bus i.

In order to introduce the control scheme, the concepts of frequency droop control must be discussed briefly. In essence, droop control uses active power injection at generator buses as a method to control frequency. The derivation begins with the equations for real and reactive power transmission across a lossless line (shown in equations (16) and (17)) with impedance X, bus 1 voltage V_1, bus 2 voltage V_2, and power angle δ.

$$P = \frac{V_1 V_2 sin(\delta)}{X} \tag{16}$$

$$Q = \frac{V_2(V_2 - V_1 cos(\delta))}{X} \tag{17}$$

Letting $sin(\delta) \approx \delta$ and $cos(\delta) \approx 1$, we have

$$\delta \approx \frac{PX}{V_1 V_2} \tag{18}$$

and

$$V_2 - V_1 \approx \frac{QX}{V_2} \tag{19}$$

Finally, the equations for frequency and droop control may be developed so that by servoing active power, δ (and hence frequency) can be controlled. Similarly, reactive power of the bus, and hence bus voltage, can be controlled. Let the nominal value of a variable be denoted by the subscript '0' (i.e. $f_0 = 60$ [Hz], the nominal frequency of the system.) Then, frequency and voltage droop control can be implemented using equations (20) and (21).

$$\Delta P_i = -\frac{\Delta f_i}{R_i},\ i = 0, 1, ..., M \tag{20}$$

where $\Delta P_i = (P_i - P_0)$, $\Delta f_n = (f_i - f_0)$, R_i is the 'frequency droop gain' at bus i, and M is the number of buses to be controlled. Similarly,

$$\Delta Q_i = -G_v \Delta V_i,\ i = 0, 1, ..., M \tag{21}$$

where $\Delta Q_i = (Q_i - Q_0)$, $\Delta V_n = (V_i - V_0)$, G_v is the 'voltage droop gain', and M is the number of control buses. Equations (20) and (21) are simply linear equations, and can be interpreted as when the system frequency decreases from its nominal value f_0 to f_i, the active power of the generator is required to increase from P_0 to P_i in a linear fashion, proportional to a chosen gain value (i.e. the slope of the line). Similarly, this rationale can be applied to reactive power output for voltage droop control.

Using a Taylor's series expansion to linearize and implementing a derivative filter with constant T_0 small, we can write the second state vector as

$$\dot{x_2} = -D_{T_0} x_2 - \frac{1}{\omega_0} D_{T_0}^2 C_1 x_1 \tag{22}$$

and

$$\Delta P = D_R x_2 - \frac{1}{\omega_0} D_R C_1 x_1 \tag{23}$$

where $\omega_0 = 2\pi f_0$, $D_{T_0} = \left(\frac{1}{T_0}\right)_{MxM}$, and $D_R = \left(\frac{1}{R}\right)_{MxM}$.

Similarly, the voltage droop control can be written in matrix format as in equation (24)

$$\Delta Q = -D_G C_2 x_1 \tag{24}$$

where $D_G = diag(G_v)_{MxM}$.

Now, combining the state space equations (13), (14), and (15) with (23) and (24), the final closed-loop system state space representation can be determined. First,

$$\dot{x_1} = \hat{A}x_1 - B_1 D_R x_2 \tag{25}$$

where $\hat{A} = A - \frac{1}{\omega_0 T_0} B_1 D_R C_1 - B_2 D_G C_2$, and combining (22) with (25), (14), and (15), the final closed-loop linear system can be expressed in (26).

$$\begin{bmatrix} \dot{x_1} \\ \dot{x_2} \end{bmatrix} = \left[\begin{array}{c|c} \hat{A} & -B_1 D_R \\ \hline \frac{1}{\omega_0} D_{T_0}^2 C_1 & -D_{T_0} \end{array}\right] \begin{bmatrix} x_1 \\ x_2 \end{bmatrix} + \left[\begin{array}{c} B_1 \\ \hline \varnothing \end{array}\right] P_{ref} + \left[\begin{array}{c} B_2 \\ \hline \varnothing \end{array}\right] Q_{ref} \tag{26}$$

In order to synthesize the controllers and demonstrate the control scheme using photovoltaic (PV) plants, the real and reactive power injected at any particular generation bus in the minni-WECC model is controlled using the closed-loop state space representation of the system, given in (26). Once the control gains are calculated for a given amount of photovoltaic penetration, the closed loop system can be modeled quite compactly. In order to demonstrate the small signal stability of the system, the eigenvalues of the plant matrix can be investigated both before and after adding solar generation to the model, and the associated movement of the eigenvalues of the system can be tracked based on the control gains.

It is important to note that the minni-WECC model maintains stability in an absolute sense as the solar penetration increases to roughly 75%, with no additional control needed (simulation results are presented in the next section). However, beyond this amount of penetration, it is necessary to implement control action to maintain stability. Because photovoltaic generators are displacing traditional electromechanical generation in this model, the implication is that the system will eventually have too little damping torque to maintain synchronism across generating units, and the system's small-signal stability will no longer be intact. It is also demonstrated that an effective control scheme derived using the basic equations for power transmission across a lossless line can alleviate some of this problem and allow a higher penetration of photovoltaics to be connected to the grid. The model will attain much higher penetration levels ($\geq 95\%$) when distributed frequency and voltage droop control is implemented. The next section presents small signal and transient stability results for the minni-WECC as the amount of PV generation is varied.

3.3 Small Signal and Transient Analysis with Minimal Controls

As mentioned in the previous section, the minni-WECC model was able to incorporate up to 75% solar generation without any additional controls. The eigenvalues as a function of solar penetration are shown in Figure 7. The solar penetration levels simulated are: 0%, 10%, 20%, 30%, 40%, 50%, 60%, 70%, and 75%. The results are consistent with previous studies - increasing renewable penetration results in an increase in mode frequency as renewable generation displaces the inertia of traditional generation. The blue line

represents a constant damping ratio ($|\Re(\lambda)|/|\lambda| = constant$). An oscillatory system has a damping ratio of 0. The larger the damping ratio, the quicker oscillations decay after a perturbation. The blue 'x' represents the nominal case (no solar), the black 'x' represents the 75% solar case, and the trajectory of eigenvalues is shown by the green '.'s. All eigenvalues in the range ($0 < freq < 1.5$ Hz) and ($-2 < \Re(\lambda) < 0$) are plotted. The stability region is given by $\Re(\lambda) < 0$. However, in reality modes with damping less than approximately 8% are considered problematic (e.g., getting close enough to the stability boundary that a small system change might result in instability). The red circles highlight the nominal North-South WECC modes. While the reduced-order minni-WECC model captures the behavior of the two primary North-South modes, the fidelity of the model is likely insufficient to draw any conclusions about the East-West mode behavior identified in a previous study [11] because the amplitude of the East-West mode is much smaller (and therefore more prone to modeling errors in a simplified model). The transient response of

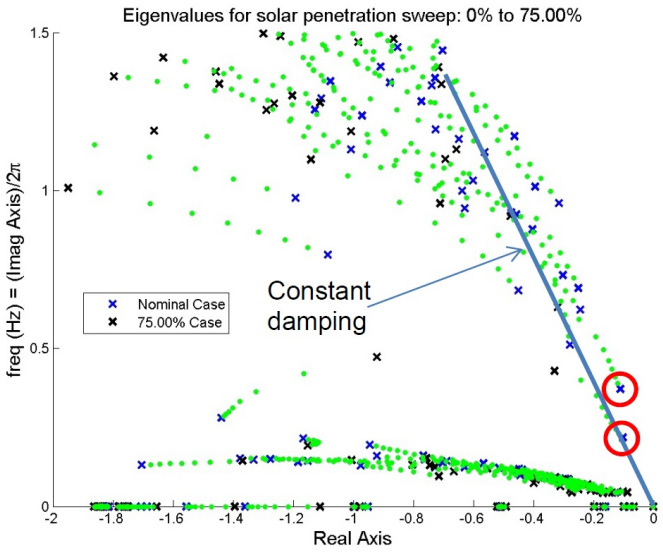

Figure 7: Minni-WECC eigenvalues as solar penetration goes from 0% to 75%, no controls case.

the minni-WECC model in response to a Palo Verde (PV) generator drop (1.4 GW) with varying solar penetrations is summarized in Figure 8. As expected, the frequency nadir is lower with increased PV generation. In addition, the reduction in system inertia results in a faster decrease in system frequency with increasing PV generation. The same information is summarized in Table 2.

Above 75% PV generation, some controls were required for the system to be stable. Adding local frequency droop and voltage support, described by equations 20 - 21, enabled PV penetrations up to 93%. The transient response for $R = 0.05$ and $Gv = 20$ is summarized in Figure 9. Increasing the gain of the frequency droop to $R = 0.01$ improves (increases) the value of the steady state system frequency after the generation drop. This is illustrated in Figure 10. Since the gain value R is in the denominator, a smaller value results in a larger overall gain.

These results are consistent with the Western Wind and Solar Integration Study (WWSIS). The WWSIS is a DOE sponsored effort to assess the impact of high penetrations of renewable generation on the western U.S. power grid [4]. The most recent phase investigated the impact of high renewable generation combined with low synchronous generation (e.g., significant coal plant retirement) [5]. The study found that increasing levels of renewable generation could be handled with traditional mitigation techniques, except for the highest penetration case. For the most extreme scenario, a system separation was observed

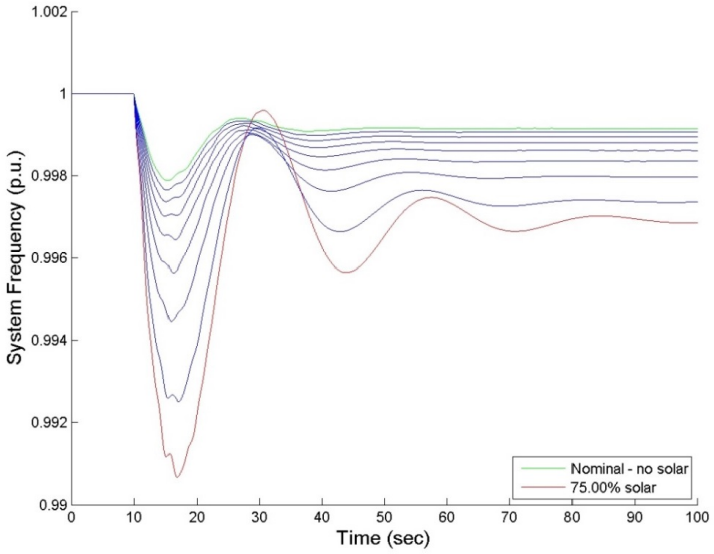

Figure 8: Minni-WECC transient response to a Palo Verde drop (1.4 GW) at t=10 sec, no controls case.

Table 2: Minni-WECC transient response to a Palo Verde drop (1.4GW) at t=10 sec, no controls case.

% Solar Generation	**Frequency Nadir (p.u.)**	**Nadir Time (sec)**	**Steady State Frequency (p.u.)**
0.00%	0.99788	15.43 sec	0.9991
10.00%	0.99765	15.30 sec	0.9991
20.00%	0.99737	15.18 sec	0.9989
30.00%	0.99701	15.05 sec	0.9988
40.00%	0.99644	16.60 sec	0.9986
50.00%	0.99564	16.32 sec	0.9984
60.00%	0.99447	15.97 sec	0.9980
70.00%	0.99251	17.11 sec	0.9974
75.00%	0.99067	6.86 sec	0.9969

in response to a fault. The behavior was primarily attributed to transient voltage collapse rather than machine angular transient stability. The study found that the results were highly dependent on: the load models; wind power plant models; and wind power plant control features. The study also noted that higher functionality wind power plants (e.g., additional controls), tended to reduce the need for other traditional mitigation [5]. Because this study employed a reduced order model of the WECC, and many of the implementation difficulties are often a local phenomenon, it is difficult to draw a conclusion on what percentage of PV generation will start to cause problems. Instead, the conclusions of eigenvalue movement and decreasing frequency nadir are the main takeaways, and are consistent with other studies.

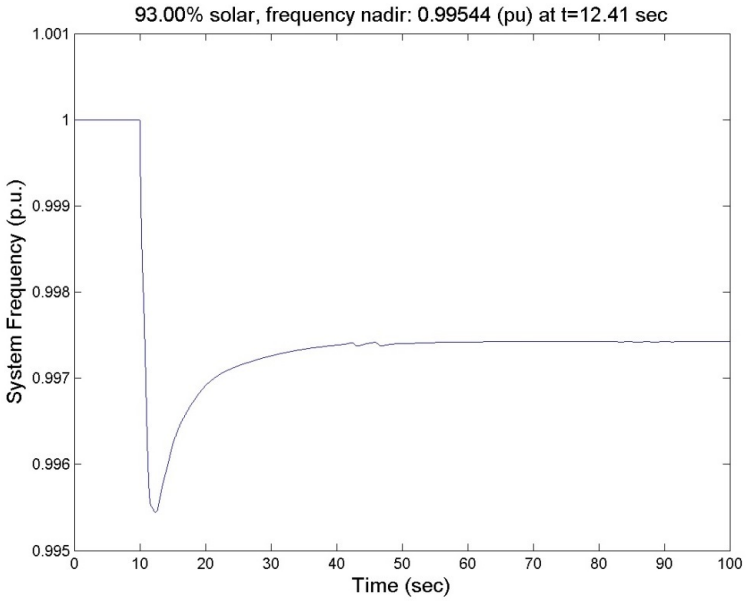

Figure 9: Minni-WECC transient response to a Palo Verde drop (1.4GW) at t=10 sec, 93% solar penetration. R = 0.05, Gv = 20. Steady state system frequency: 0.9953.

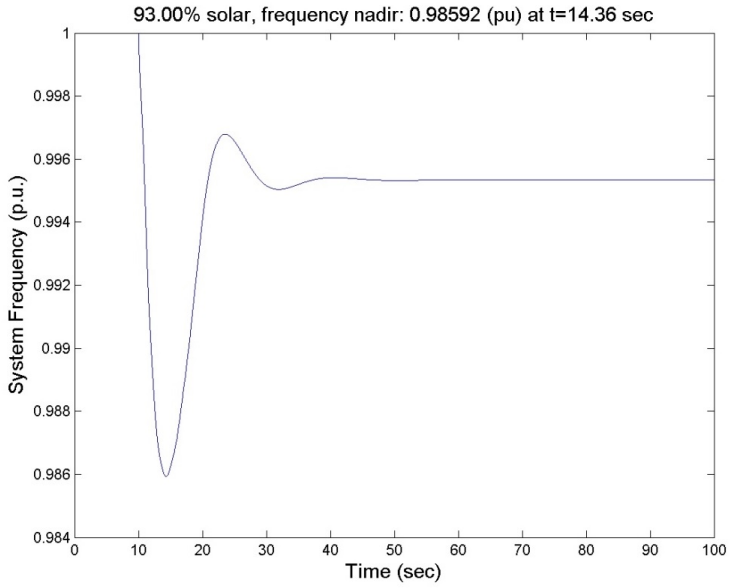

Figure 10: Minni-WECC transient response to a Palo Verde drop (1.4GW) at t=10 sec, 93% solar penetration. R = 0.01, Gv = 20. Steady state system frequency: 0.9974.

3.4 Fixed Structure Optimal Control

The Fixed structure control development for mitigating frequency deviations across the grid begins with the development of the small-signal model and the identification of an appropriate algorithm. In this section, these steps are presented and then applied to a minni-WECC example.

It is common for the small-signal dynamic behavior of large power systems to be described using linear models [27]. In particular, when linearized about an operating point, the power system dynamics may be represented as the state space model

$$\dot{x}(t) = Ax(t) + B_d u_d(t) + B_e u_e(t) \tag{27}$$

$$y(t) = Cx(t) \tag{28}$$

where $x \in \mathbb{R}^n$ is the system state vector, which includes small-signal rotor angle and speed deviations among other quantities, $u_d \in \mathbb{R}^p$ is the input vector of real power injection intended to provide system damping, and $u_e \in \mathbb{R}^m$ is an exogenous input that may represent probing signals or other inputs designed to excite a system response [27]. For damping control, the output vector $y \in \mathbb{R}^h$ is a vector of generator speeds available for feedback.

The stability of the system is described by the eigenvalues of the $n \times n$ matrix A, and the mode shape is encoded into the eigenvectors of A. Elements of the $n \times p$ matrix B_d would be determined by the location and interconnection of distributed damping control resources. The goal herein is to compute a $p \times h$ damping controller gain matrix K_d such that the eigenvalues of $A - B - dK_dC$ are further left in the complex plane, indicating improved damping. Furthermore, the selection of gain values should account for priorities concerning performance and control energy expended by the distributed resources. These priorities are represented using a performance index.

The performance index, or cost function, is given as follows

$$J = \int_0^\infty \left(y^T Q y + U_d^T R u_d \right) dt \tag{29}$$

wherein the term $y^T Qy$ assigns a penalty for the state trajectory with $Q \geq 0$, and $u_d^T R u_d$ penalizes the control energy with $R > 0$. For a damping control application $y^T Qy$ would be formulated to penalize frequency error (local and/or inter-area). The control design problem is thus to select the controller gain matrix K_d so as to minimize J. The problem resembles the familiar *linear quadratic regulator* (LQR) problem wherein an optimal K_d is computed analytically through solution of the algebraic Riccati equation for full state feedback. In this application however, full state feedback is not required or desired, and it cannot be assumed the pair (A, B_d) is controllable. Thus, the LQR solution is not used directly to compute K_d; rather the solution is attained numerically.

The optimal gain is computed using an iterative numerical method based on the Anderson-Moore descent function [17, 28]. which allows for feedback signals to be excluded from the optimal solution. The system model and performance metric, however, must be augmented to enable this approach. The damping controller inputs are partitioned into p areas/subsystems wherein

$$B_d u_d = \sum_{i=1}^{p} B_{d,i} u_{d,i} \tag{30}$$

$$u_{d,i} = K_{d,i} C_i x, \; i \; \in \{1, 2, \ldots, p\} \tag{31}$$

In addition, the R matrix is assumed to be diagonal $R = diag(R_1, R_2, \ldots, R_p)$, and the control inputs are normalized such that $\tilde{u}_{d,i} = \sqrt{R_i} u_{d,i}$ where $u_{d,i}$ is the i^{th} element of u_d .

Second, an additional cost term is formulated to penalize the use of unavailable or undesired feedback signals, and the term is added to the cost function, resulting in the expression

$$\tilde{J} = \int_{t_0}^{\infty} \left(y^T Q y + \tilde{u}_d^T \tilde{u}_d \right) d\tau + ||\tilde{K}_{d,i} \Gamma_i C_i x||^2 \tag{32}$$

where $\Gamma_i \geq 0$ is a diagonal matrix of weights that penalizes feedback of select signals. The optimal damping control problem may be summarized as follows

$$\begin{aligned} &\text{minimize } \tilde{J} \\ &\quad \tilde{K}_d \\ &\text{subject to:} \\ &(1)\ \dot{x}(t) = \left(A - B_d \tilde{K}_d C \right) x(t) \\ &(2)\ Q \geq 0 \\ &(3)\ \Gamma_i \geq 0 \end{aligned}$$

The gain matrix K_d is then determined through proper scaling of $\tilde{K}_d$.

To solve the above optimization problem, a numerical algorithm is used to iteratively approach the solution. The algorithm requires the calculation of some intermediate quantities. In each iteration, $\tilde{K}_{d,i}$ values are updated and the system $A-$matrix is updated.

$$A_0 = A + \sum_{i=1}^{p} B_{d,i} \tilde{K}_{d,i} C_i \tag{33}$$

Likewise, the Q matrix is extended to include the control signal penalties according to

$$Q_0 = Q + \sum_{i=1}^{p} \left(C_i^T \tilde{K}_{d,i}^T \tilde{K}_{d,i} C_i + C_i^T \Gamma_i^T \tilde{K}_{d,i}^T \tilde{K}_{d,i} \Gamma_i C_i \right) \tag{34}$$

In each iteration, the gain matrix is incremented by a quantity computed according to

$$\Delta \tilde{K}_{d,i} = -\tilde{K}_{d,i} - B_{d,i}^T P X C_i^T \left(C_i X C_i^T + \Gamma_i C_i X C_i^T \Gamma_i^T \right)^{-1} \tag{35}$$

where X is the state covariance matrix.

Algorithm 1 Structured Control Algorithm

Initialize the state Covariance X_0
Initialize K_d by solving the LQR problem, and segment into p rows: $u_{d,i},\ i \in \{1, 2, \ldots, p\}$
while change in gain is above tolerance $\Delta||K_d||_\infty > tol$ **do**
  Compute A_0 using Equation (33)
  Solve $X_0 + X A_0^T + A_0 X = 0$ for X
  Compute Q_0 using Equation (34)
  Solve $Q_0 + P A_0 + A_0^T P = 0$ for P
  Compute new gain $\tilde{K}_{d,i} + \alpha \Delta \tilde{K}_{d,i}$ using Equation (35)
end while
Compute $K_{d,i} = \dfrac{\tilde{K}_{d,i}}{\sqrt{R_i}},\ \forall i \in \{1, 2, \ldots, p\}$

The intention is that this algorithm can compute gains that result in a more optimal allocation of control energy. This would be useful for utilities that wish to realize prioritized wide area damping control given limited resources, i.e. PV curtailment or energy storage. The next section presents results for a reduced order model of the WECC.

3.4.1 Minni-WECC Scenario: Damping the East-West Mode

To demonstrate the algorithm, it is convenient to consider again the nominal mini-WECC model (0% PV) and a relevant damping scenario. Assuming a damping control resource may be installed at each bus hosting a generator, a cost function is formulated to penalize the nominally 0.5 Hz East-West oscillations in particular. The Mode shape is illustrated in Figure 11. Therein, generators/buses marked with a red dot are oscillating against those marked with a blue dot. The diameter of the dot provides an indication of the amplitude of participation in the given mode.

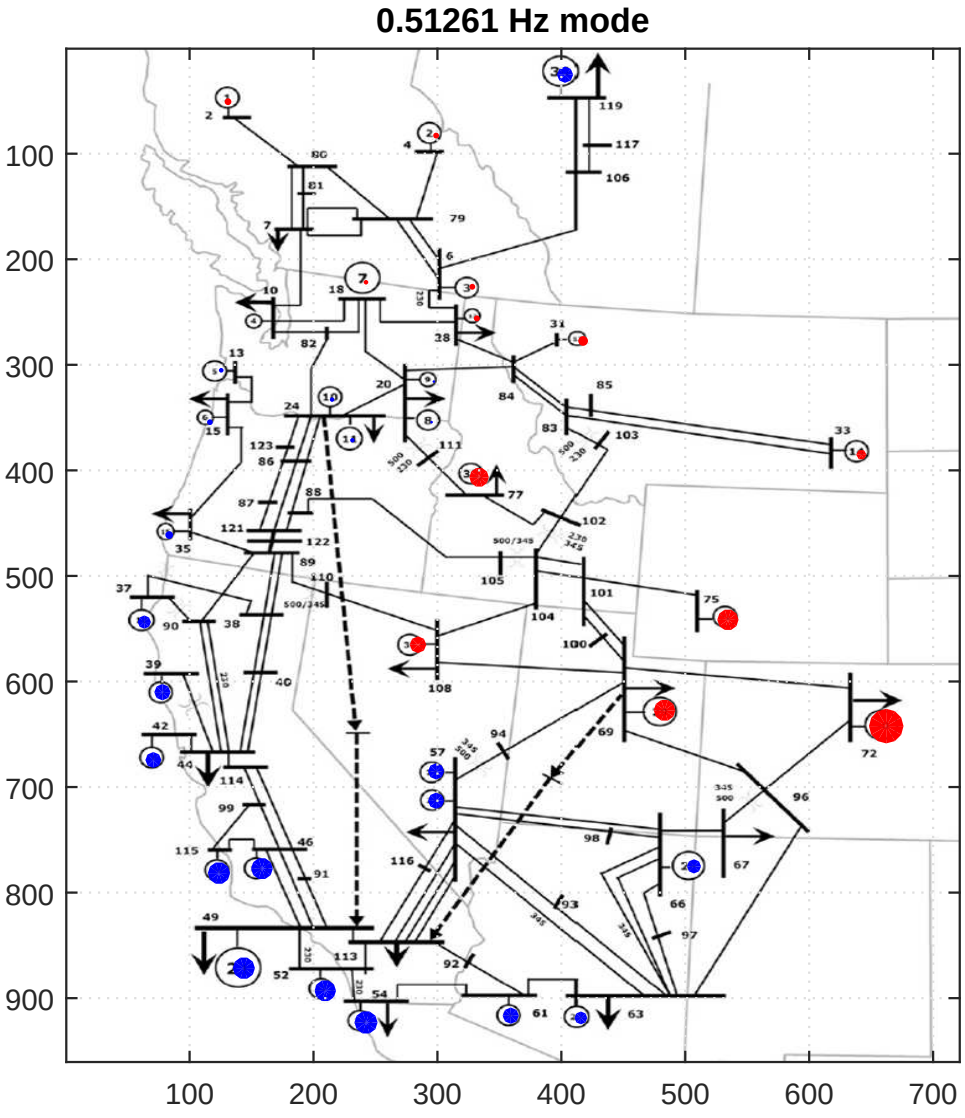

Figure 11: East-West mode shape: buses marked by a red dot are oscillating against those marked by a blue dot, and dot diameter indicates the magnitude of participation in the mode

The cost function is given as the linear combination of the generator speeds, squared and is designed to isolate the energy in this particular mode. The cost function is formulated as follows

$$y^T Q y = \left(\sum_{i=1}^{N} k_i \omega_i \right)^2 \tag{36}$$

where

$$\sum_{i=1}^{N} k_i = 0 \tag{37}$$

The k_i values are computed using terms from the right eigenvector (which contains mode shape information) with a projection method that ensures the values sum to zero. The values used to isolate the East-West mode are shown graphically in Figure 12.

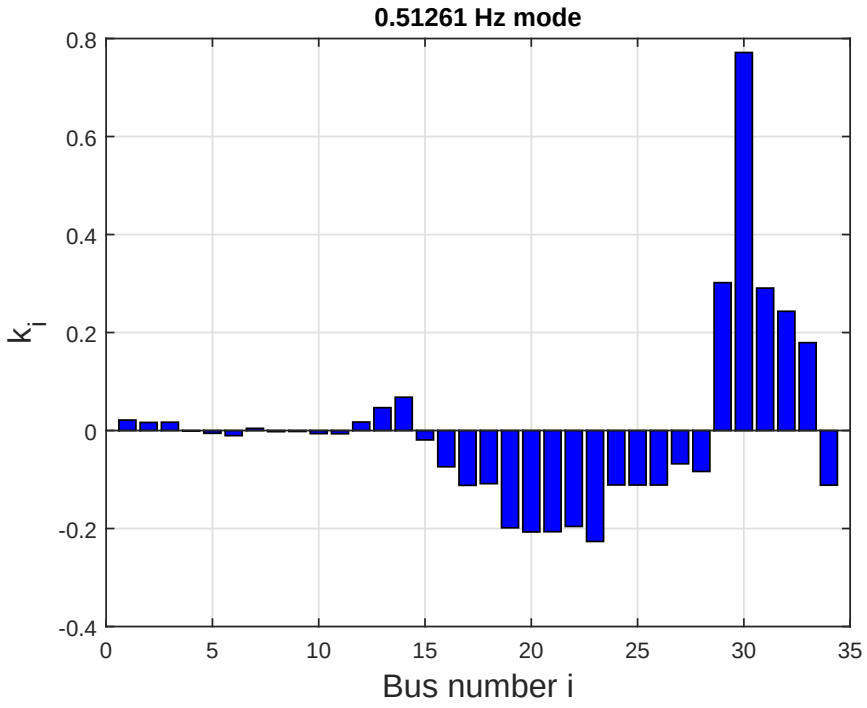

Figure 12: Weighting terms used in the cost function.

Algorithm 1 was utilized to compute the optimal gains for two implementation scenarios: local and networked (local plus remote) frequency feedback. For the local feedback scenario, the Γ matrix was configured to provide no additional penalty for control energy based on local feedback but to penalize control energy based on remote signal feedback. The resulting controller gains are shown in Figure 13. Therein the damping K gains as determined by Algorithm 1 are shown both as an image of the gain matrix where off-diagonal values are zero (shown as grey) and as a bar graph, clarifying the sign of the gain values. The units are given in per-unit (ie. scaled by base power divided by base frequency). Since typical gain values are in the MW/mHz range, the per unit quantities are rather large. Therein, one notes the damping is primarily prioritized at generators 16 through 25 and 30 through 34 which corresponds closely to the key generators identified in Figure 11. Furthermore, it is noted that two of the gain values are actually negative, indicating a positive local feedback; this would be difficult to implement in practice.

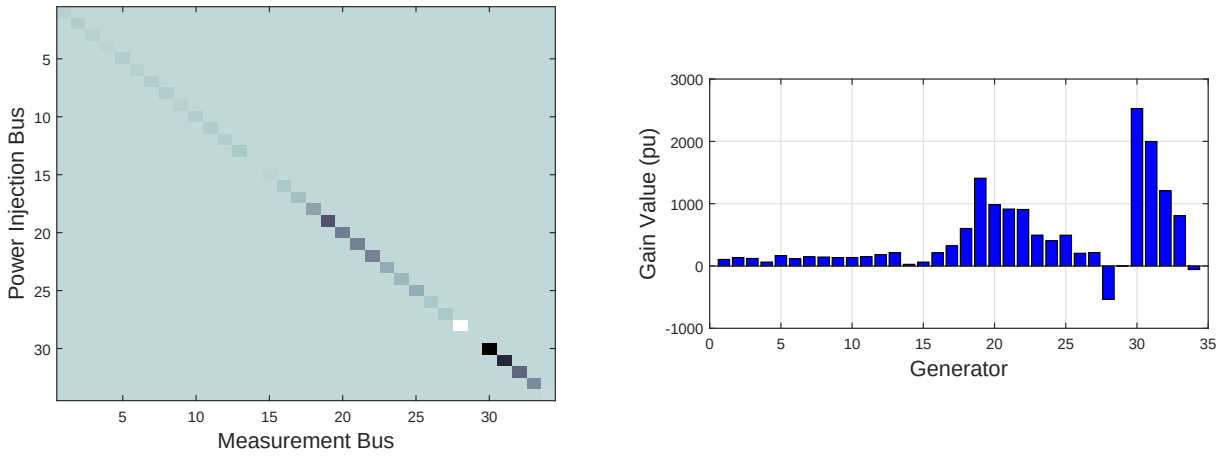

Figure 13: Damping K gains as determined by Algorithm 1 shown (left) as an image of the gain matrix: gray = 0, black = negative, white = positive and (right) as a bar graph .

To evaluate the effect of these optimal gain selections, the root locus is shown in Figure 14. Therein, the blue Xs indicate the eigenvalues without control and the red Xs indicate the eignevalues with the gain matrix as computed. The red dots are attained by scaling the gain matrix by numbers that vary from 0 to 1. It is noted that the targeted mode at 0.5 Hz (approximately 3.14 radians/sec) exhibits much improved damping. Other modes also show some improvement, however, some reduced damping is seen in modes at 0.67 Hz and at 0.97 Hz. The 0.67 Hz mode is likely the Alberta mode, and the 0.97 Hz mode is likely generator 28 swinging against the rest of the system due to positive local feedback. Since only local feedback was used, the ability to isolate the effect to one mode is limited, and the risk of worsening other modes is plausible. Since the actuation is distributed, controllability should not be an issue. Rather, distributed feedback may instead provide an improved response. This motivates the use of Networked information (from a WAMS-like network). Comparing to Figure 14 to Figure 7, Figure 7 illustrates the eigenvalues of the system with no additional controls as the percentage of PV is increased. Figure 14 shows the eigenvalue movement for a particular PV penetration (0% for this case) as the damping gains are adjusted by Algorithm 1. Note that the targeted mode (eigenvalue) is moved to the left with minimal impact to other eigenvalues.

Using the minni-WECC model, the control goal is now to dampen the East-West mode at approximately 0.5 Hz using wide area feedback. For the wide area feedback scenario, the Γ matrix does not include any penalties for frequency feedback. This allows for each control to use feedback from any of the 34 bus frequency sensors. The feedback gain matrix, as computed by Algorithm 1, is illustrated in Figure 15. Therein, local and remote feedback is included with diagonal elements representing the local feeback and off-diagonal elements being remote signals with black being negative and white being positive. Contrasting this image with that in Figure 13 illustrates the difference. It is further noted in Figure 15 that a definite structure is present with select buses being modulated against one another, and these correspond strongly with what would be expected through study of Figure 11.

The eigenvalue plot for wide area feedback is given in Figure 16. The benefit of wide area feedback over local feedback is clear, wide area feedback results in greatly improved damping of the 0.5 Hz mode and slight improvements in other modes without worsening the damping of any modes. Additional results on optimal fixed structure control applied to the frequency-watt inverter function can be found in [29].

To demonstrate the effect of this control in the time-domain, the minni-WECC model was simulated

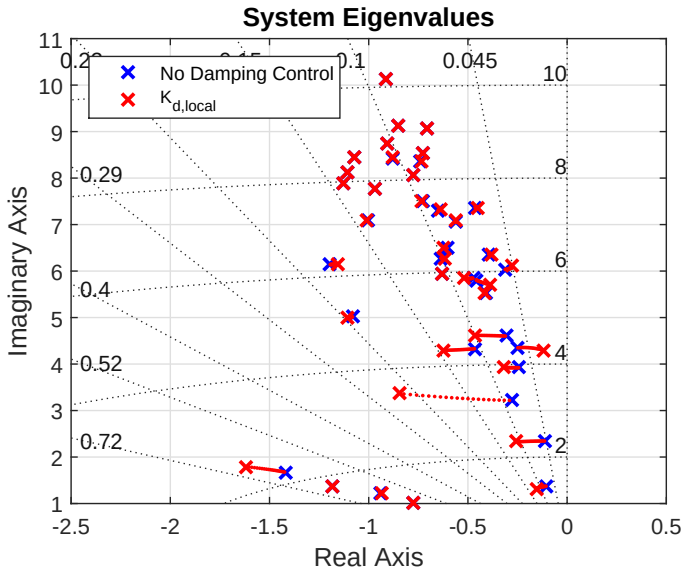

Figure 14: Minni-WECC eigenvalues as damping K gains are adjusted by Algorithm 1.

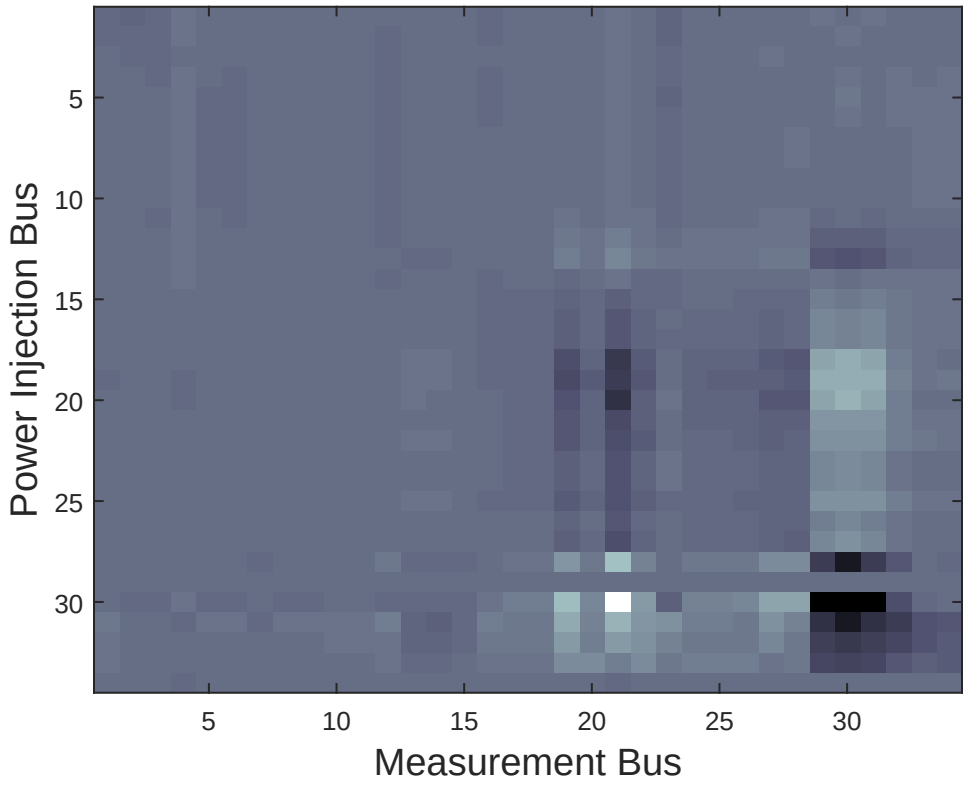

Figure 15: Visualization of gain matrix with wide area feedback: gray = 0, black = negative, white = positive.

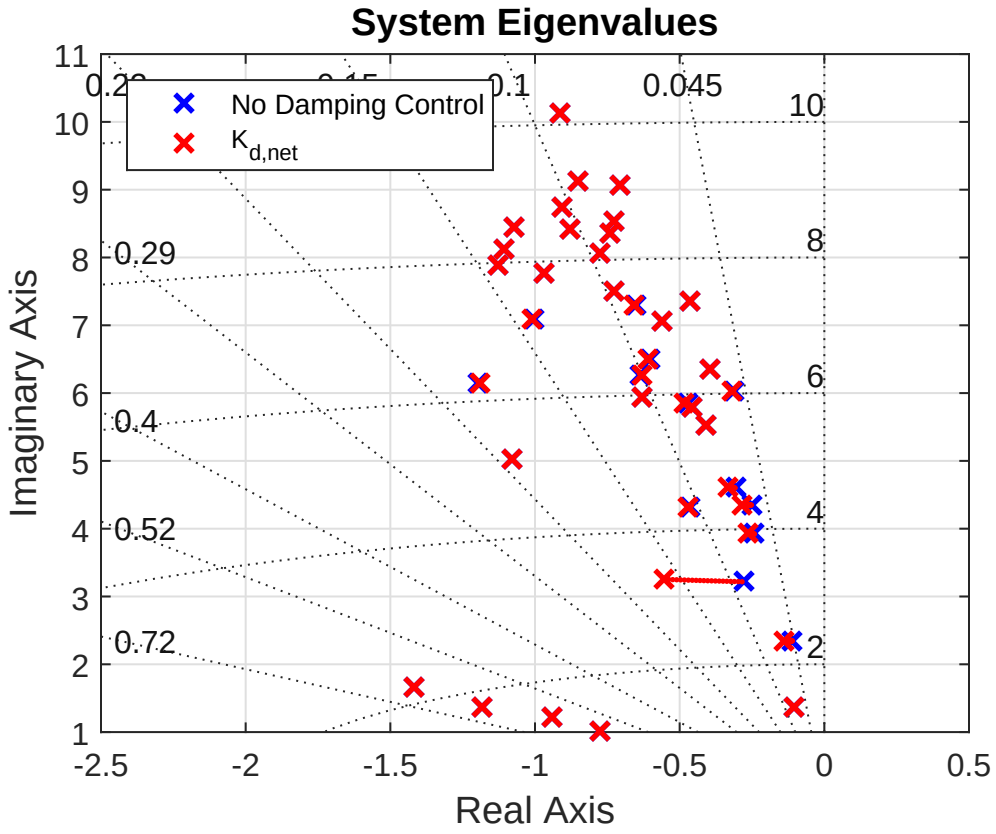

Figure 16: East-West mode damping with wide area feedback.

with and without the Networked damping control. The simulation runs for 40 seconds with a simulated loss of generation at the Palo Verde plant. This causes a large depression in the generator speeds and excites an inter-area oscillation that includes several modes including the East-West mode. To illustrate the East-West mode in particular, it is convenient to focus on the generators 19 and 30 and the difference in generator speeds between them. Figure 17 shows the generator response following this event with no added controls. Therein, the speeds for generators 19 and 30 reach a nadir of 59.58 Hz and 59.56 Hz respectively, and the two machines are visibly oscillating against one another. Figure 18 shows the generator response following this event with added damping controls and Network feedback given by the gain matrix depicted in Figure 15. The frequency nadir is much improved; generators 19 and 30 reach a nadir of 59.87 Hz and 59.85 Hz respectively. This may be due to the local feedback element of the control effectivley contributing to the droop response. Figure 19 shows the differences in generator speed errors in the controlled and uncontrolled cases. This response is dominated by the East-West mode. The value of the damping control is immediately evident. For the uncontrolled case, the peak speed error is 60.4 mHz, and the system persists ringing for nearly the whole simulation. For the case with damping control, the speed error peak is reduced to 25.4 mHz, and the ring-down event is seen to extinguish is approximately 7 seconds.

This section demonstrated the application of the structured control approach to a real-life damping control problem in the minni-WECC model. The example illustrates how the approach can enable precise changes to the eigenvalues of the system, and the time domain simulation demonstrates the improvement to oscillation response. The next section discusses some observations on the relationship between phase margin and damping ratio in multi-mode systems.

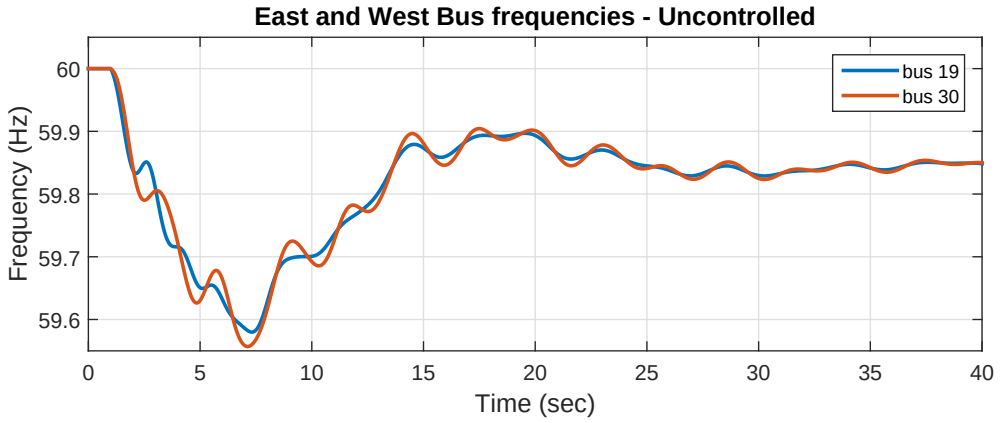

Figure 17: Generator speeds following a simulated loss of Palo Verde without added damping controls

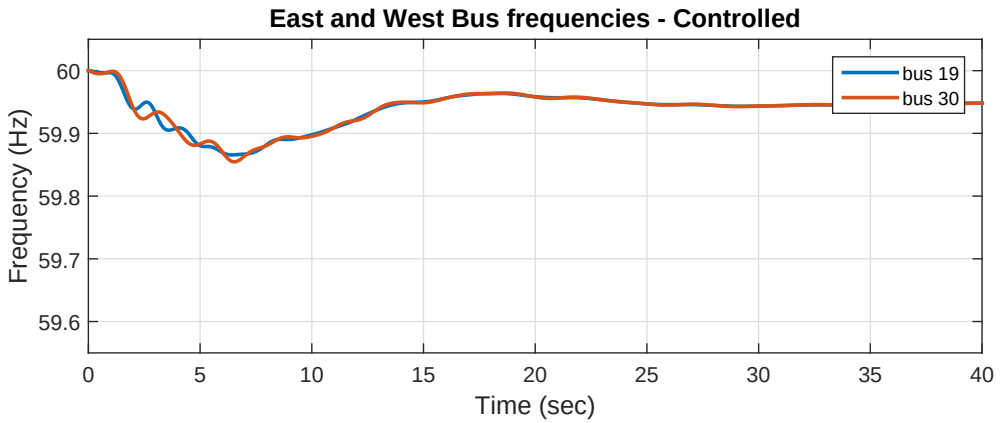

Figure 18: Generator speeds following a simulated loss of Palo Verde with added damping controls

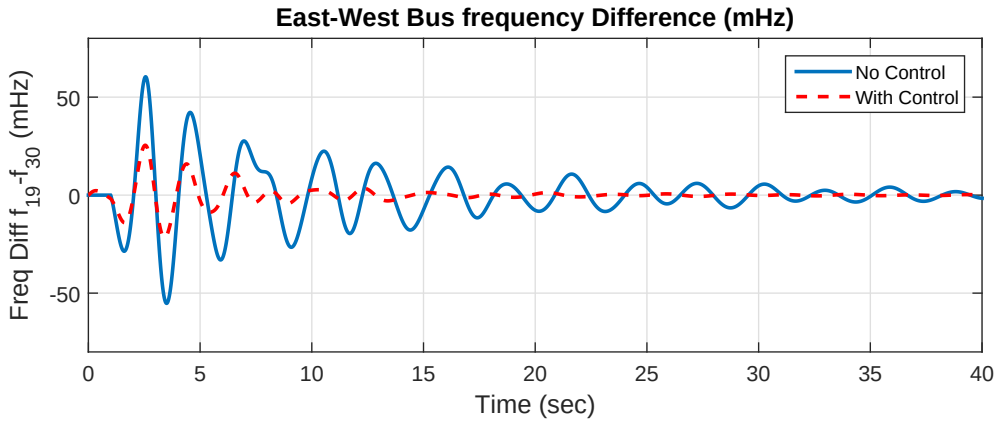

Figure 19: Generator speed differences following a simulated loss of Palo Verde with and without added damping controls

3.4.2 Phase Margin in Multi-Mode Systems

To aid in interpreting results, a brief investigation was done into the dependency of phase margin (PM) on damping in multi-mode systems. Consider a second order system with a stable pole and a pole at the origin

$$G(s) = \frac{\omega^2}{s\left(s + 2\zeta\omega\right)} \tag{38}$$

Phase margin is defined as the difference in phase from 180 degrees at unity feedback. If unity feedback is applied, the closed-loop transfer function is given by

$$T(s) = \frac{G(s)}{1 + G(s)} = \frac{\omega^2}{s^2 + 2\zeta\omega s + \omega^2} \tag{39}$$

The phase margin may be computed explicitly as

$$\text{PM} = \tan^{-1}\left(\frac{2\zeta}{\left(\sqrt{1 + 4\zeta^4} - 2\zeta^2\right)^{1/2}}\right) \tag{40}$$

Equation (40) was then evaluated over a range of damping ratios and compared to the Matlab **margin()** function. The results are found in figure 20. The phase margin is approximately linear in the damping ratio up to a damping ratio of 0.6 and a phase margin of 60 degrees regardless of natural frequency ω. For

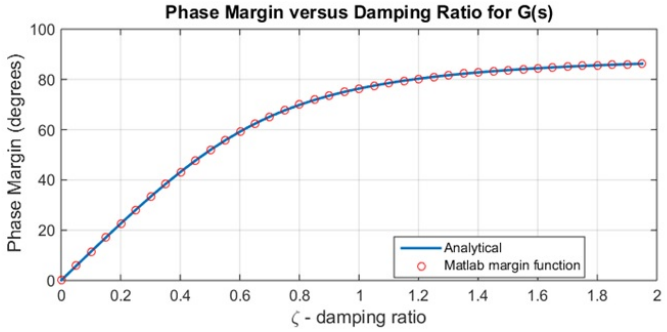

Figure 20: Phase margin versus damping ratio for a second order system.

a three-area system, there are two modes and an analytical expression for phase margin is more difficult to attain. Therefore, this was analyzed using only Matlab with a model having no zeros. The open-loop system transfer function was assumed to be

$$G_{2m}(s) = \frac{\omega_1\omega_2}{s\left(s^3 + 2(\zeta_1\omega_1 + \zeta_2\omega_2)s^2 + (\omega_1^2 + \omega_2^2 + 4\zeta_1\zeta_2\omega_1\omega_2)s + 2\zeta_1\omega_1\omega_2^2 + 2\zeta_2\omega_1^2\omega_2\right)} \tag{41}$$

To illustrate an example, the frequencies ω_1 and ω_2 were selected to coincide with realistic oscillatory mode frequencies and the phase margin was computed in Matlab for a range of damping values. A 3D surface plot is shown in Figure 21. Therein, it is noted that the phase margin benefits more from increases in ζ_1 , the lower frequency damping coefficient. This is verified in Figure 21 wherein damping coefficients corresponding to PM=9 degrees were identified, forming a line whose slope indicates that greater increases in ζ_2 than in ζ_1 are needed to accomplish the same phase margin. In fact, the difference is quite considerable despite the small difference in frequency. This suggests that, under certain circumstances, phase margin stability margins may be predicted from estimates of damping coefficients for the lowest frequency modes.

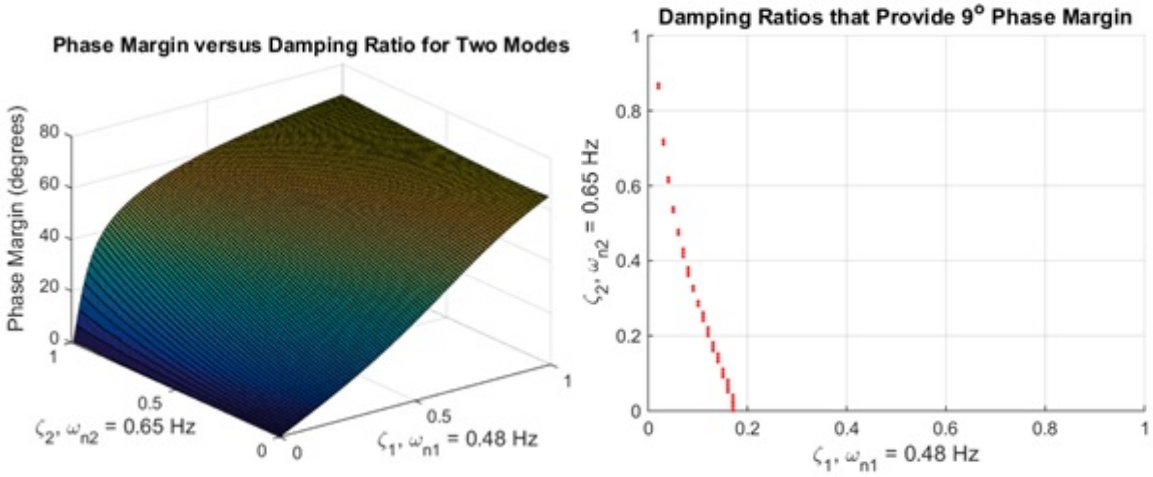

Figure 21: Relationship of Phase Margin to damping values in an example two-mode system showing (a) 3D surface plot of PM vs ζ_1 and ζ_2 and (b) line of ζ_1 and ζ_2 values that give a PM of 9 degrees.

3.5 Nyquist Stability Methods

The Nyquist stability criterion is a vital tool to examine the small signal stability of the system. The criterion is based on the Nyquist contour mapped through the function $G(s)$ where $G(s)$ is the open loop transfer function of the system of interest. The Nyquist contour is a D-shaped region that encircles the left half plane. The stability criterion is summarized below:

Nyquist Stability Criterion: A system $G(s)$ is stable if the Nyquist contour $\Gamma_{G(s)}$ encircles (clock-wise) the -1 point N times, where $N = Z - P$ where Z is the number of open-loop poles in the right-half-plane (RHP) and P is the number of open-loop zeros in the right-half-plane.

The next section applies the Nyquist stability criterion to a three-area power system model with time delay.

3.5.1 Three-Area Model

To begin the analysis it is helpful to examine a simplified three area model as shown in Figure 22. The model parameters are defined in the table below. First, a state space model of the system was constructed

Table 3: Three-Area System Model Quantities

Quantity	Description
M_i	Area i inertia
D_i	Area i damping
T_{ij}	Synchronizing torque coefficient between area i and j
ΔP_{Li}	Area i load variation
ΔP_{Di}	Area i damping torque (control effort)
$\Delta\omega_i$	Area i change in speed
$\Delta\delta_i$	Area i change in angle

from the transfer function block diagram. Focusing on area 1, the area frequency, $\Delta\omega_1$, can be expressed by the differential equation:

$$\Delta\omega_1 = \frac{1}{M_1 s + D_1}\left(\Delta P_{L1} - \Delta P_{D1} + T_{31}\left(\Delta\delta_3 - \Delta\delta_1\right) - T_{12}\left(\Delta\delta_1 - \Delta\delta_2\right)\right) \tag{42}$$

Rearranging (42) to solve for the first derivative of $\Delta\omega_1$ will result in:

$$M_1 s\Delta\omega_1 + D_1\Delta\omega_1 = \left(\Delta P_{L1} - \Delta P_{D1} + T_{31}\left(\Delta\delta_3 - \Delta\delta_1\right) - T_{12}\left(\Delta\delta_1 - \Delta\delta_2\right)\right) \tag{43}$$

$$s\Delta\omega_1 = \frac{1}{M_1}\left(-D_1\Delta\omega_1 + \Delta P_{L1} - \Delta P_{D1} - \left(T_{12} + T_{31}\right)\Delta\delta_1 + T_{12}\Delta\delta_2 + T_{31}\Delta\delta_3\right) \tag{44}$$

A similar procedure can be done on areas two and three to get differential equations for $\Delta\omega_2$ and $\Delta\omega_3$:

$$s\Delta\omega_2 = \frac{1}{M_2}\left(-D_2\Delta\omega_2 + \Delta P_{L2} - \Delta P_{D2} + T_{12}\Delta\delta_1 - \left(T_{12} + T_{23}\right)\Delta\delta_2 + T_{31}\Delta\delta_3\right) \tag{45}$$

$$s\Delta\omega_3 = \frac{1}{M_3}\left(-D_3\Delta\omega_3 + \Delta P_{L3} - \Delta P_{D3} + T_{31}\Delta\delta_1 + T_{23}\Delta\delta_2 - \left(T_{23} + T_{31}\right)\Delta\delta_3\right) \tag{46}$$

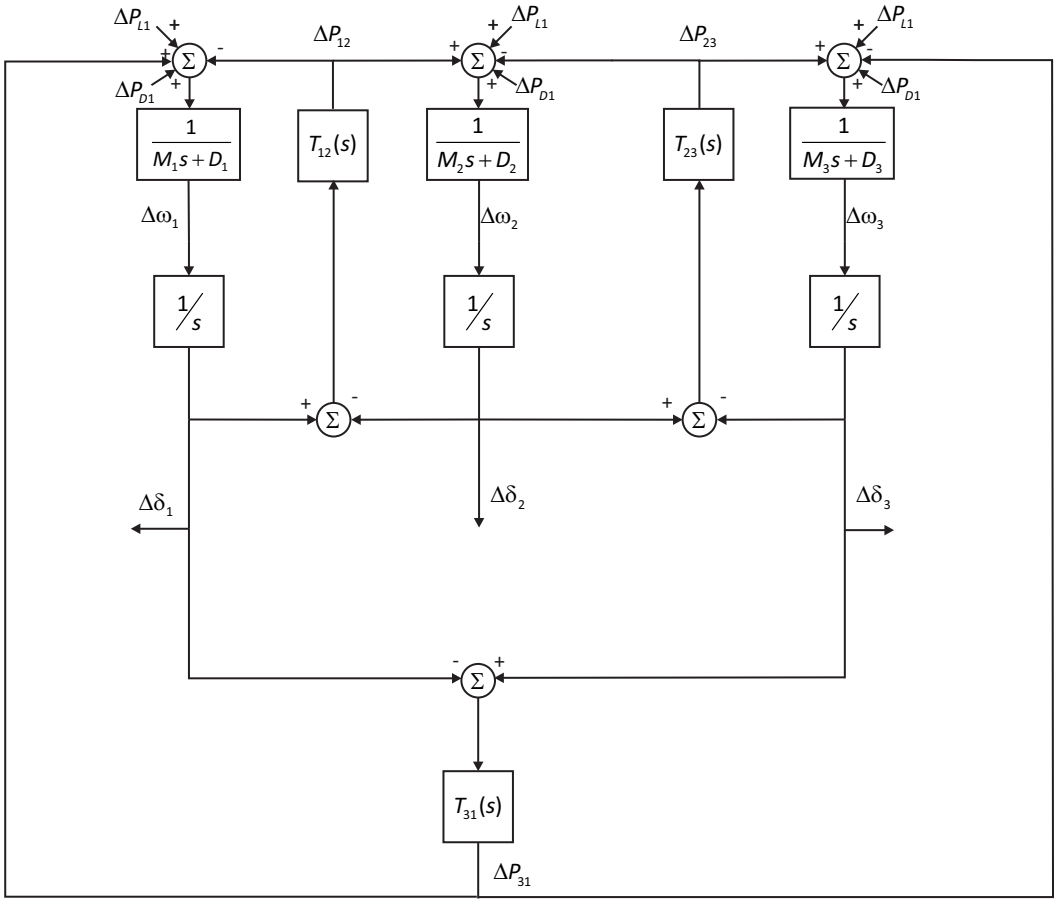

Figure 22: Three Area Model

The angle differences in each area, $\Delta\delta_1$, $\Delta\delta_2$, and $\Delta\delta_3$, can be expressed with the differential equations:

$$s\Delta\delta_1 = \Delta\omega_1 \tag{47}$$

$$s\Delta\delta_2 = \Delta\omega_2 \tag{48}$$

$$s\Delta\delta_3 = \Delta\omega_3 \tag{49}$$

using equations (44)-(49) a state space model can be constructed such that:

$$\dot{\vec{\mathbf{x}}} = \mathbf{A}\vec{\mathbf{x}} + \mathbf{B}_1\vec{\mathbf{u}}_1 - \mathbf{B}_2\vec{\mathbf{u}}_2 \tag{50}$$

$$\vec{\mathbf{y}} = \mathbf{C}\vec{\mathbf{x}} + \mathbf{D}_1\vec{\mathbf{u}}_1 - \mathbf{D}_2\vec{\mathbf{u}}_2 \tag{51}$$

Where the matrices and vectors are defined as:

$$\mathbf{A} = \begin{bmatrix} -\frac{D_1}{M_1} & -\frac{(T_{12}+T_{31})}{M_1} & 0 & \frac{T_{12}}{M_1} & 0 & \frac{T_{31}}{M_1} \\ 1 & 0 & 0 & 0 & 0 & 0 \\ 0 & \frac{T_{12}}{M_2} & -\frac{D_2}{M_2} & -\frac{(T_{12}+T_{23})}{M_2} & 0 & \frac{T_{23}}{M_2} \\ 0 & 0 & 1 & 0 & 0 & 0 \\ 0 & \frac{T_{31}}{M_3} & 0 & \frac{T_{23}}{M_3} & -\frac{D_3}{M_3} & -\frac{(T_{23}+T_{31})}{M_3} \\ 0 & 0 & 0 & 0 & 1 & 0 \end{bmatrix} \tag{52}$$

$$\mathbf{B_1} = \mathbf{B_2} = \begin{bmatrix} \frac{1}{M_1} & 0 & 0 \\ 0 & 0 & 0 \\ 0 & \frac{1}{M_2} & 0 \\ 0 & 0 & 0 \\ 0 & 0 & \frac{1}{M_3} \\ 0 & 0 & 0 \end{bmatrix} \tag{53}$$

$$\mathbf{C} = \begin{bmatrix} 1 & 0 & 0 & 0 & 0 & 0 \\ 0 & 0 & 1 & 0 & 0 & 0 \\ 0 & 0 & 0 & 0 & 1 & 0 \end{bmatrix} \tag{54}$$

$$\vec{\mathbf{x}} = \begin{bmatrix} \Delta\omega_1 \\ \Delta\delta_1 \\ \Delta\omega_2 \\ \Delta\delta_2 \\ \Delta\omega_3 \\ \Delta\delta_3 \end{bmatrix} \tag{55}$$

$$\vec{\mathbf{u}}_1 = \begin{bmatrix} \Delta P_{L1} \\ \Delta P_{L2} \\ \Delta P_{L3} \end{bmatrix} \tag{56}$$

$$\vec{\mathbf{u}}_2 = \begin{bmatrix} \Delta P_{D1} \\ \Delta P_{D2} \\ \Delta P_{D3} \end{bmatrix} \tag{57}$$

The input vector has two components separated into $\vec{\mathbf{u_1}}$ and $\vec{\mathbf{u_2}}$. The first input is based on the load torques in each area, ΔP_{L1}, ΔP_{L2}, and ΔP_{L3}, and the other is based on the damping torques in each area, ΔP_{D1}, ΔP_{D2}, and ΔP_{D3}. The damping torques supply the system feedback and can be expressed by the system of equations:

$$\Delta P_{D1} + \Delta P_{D2} + \Delta P_{D3} = 0 \tag{58}$$

$$\Delta P_{D1} = k_{d12}\left(\Delta\omega_1 - \Delta\omega_2\right) - k_{d31}\left(\Delta\omega_3 - \Delta\omega_1\right) \tag{59}$$

$$\Delta P_{D2} = k_{d23}\left(\Delta\omega_2 - \Delta\omega_3\right) - k_{d12}\left(\Delta\omega_1 - \Delta\omega_2\right) \tag{60}$$

$$\Delta P_{D3} = k_{d31}\left(\Delta\omega_3 - \Delta\omega_1\right) - k_{d23}\left(\Delta\omega_2 - \Delta\omega_3\right) \tag{61}$$

where k_{dxy} is the damping coefficient between areas x and y (e.g., controller gain). Equations (59) - (61) can be expressed in linear form in relation to the state vector as:

$$\vec{\mathbf{u}}_2 = \begin{bmatrix} \Delta P_{D1} \\ \Delta P_{D2} \\ \Delta P_{D3} \end{bmatrix} = -\mathbf{K}\vec{\mathbf{x}} = \begin{bmatrix} k_{d12}+k_{d31} & 0 & -k_{d12} & 0 & -k_{d31} & 0 \\ -k_{d12} & 0 & k_{d12}+k_{d23} & 0 & -k_{d23} & 0 \\ -k_{d31} & 0 & -k_{d23} & 0 & k_{d23}+k_{d31} & 0 \end{bmatrix} \vec{\mathbf{x}} \tag{62}$$

Because of the distances involved in inter-area communications a time delay, T_d, is added to the controller to fully analyze the stability of the model

$$\dot{\vec{\mathbf{x}}} = \left(\mathbf{A} + \mathbf{BK}\left(1 + e^{-sT_d}\right)\right)\vec{\mathbf{x}} + \mathbf{B}\vec{\mathbf{u}}_1 \tag{63}$$

The state space model was implemented in Matlab using the **delayss()** function to incorporate the damping time delay. Since there are three inputs and three outputs to the system, the **nyquist()** function

was used to find the Nyquist curves of all nine resulting transfer functions. In order to test the stability of these Nyquist curves, the ESAC criterion was applied [6]. This criterion sets up a polygon around the point $(-1, 0)$ based on a given phase and gain margin as shown in Figure 23. The Matlab function **inpolygon()** is then used to determine if any of the Nyquist curves violate the ESAC criteria. To make sure that sampling does not result in a missed detection of an unacceptable point, the zero crossings of the real axis are calculated and checked against the ESAC gain margin criterion. This procedure is repeated for a range of damping coefficients to find the volume of values that are not guaranteed stable. The results of this procedure for different values of time delay are shown in Figure 24 through Figure 27. An alternative approach would have been to visualize the regions of gains and time delays which meet the ESAC stability criterion.

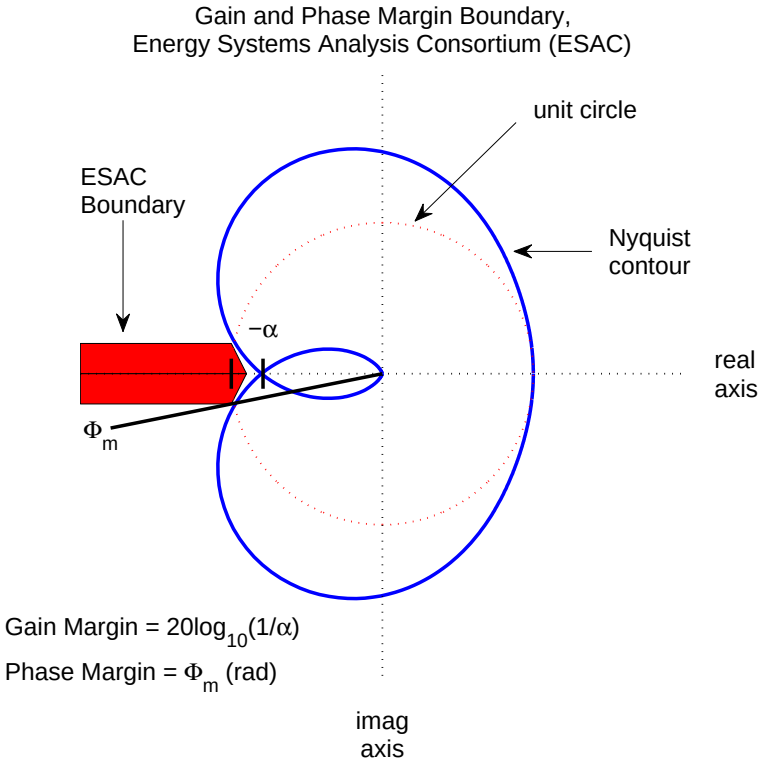

Figure 23: ESAC criterion boundary.

As shown in Figure 24, even with no time delay there is a significant region along the k_{d12}, k_{d23}, and k_{d31} axes where the Nyquist curves violate the ESAC criteria. This shows that some damping is required in the system to ensure stability. As the delay is increased, additional volumes of disallowed states start to appear, typically starting at higher values of k_{d12}, k_{d23}, and k_{d31} and moving closer to the origin as the delay increases. Eventually these volumes will increase the size of the final volume. Based on this simplified model it is clear that this method can be used to validate the stability of a given system. However, the computational needs of using the method to search for stable solutions grows exponentially with the number of damping coefficients. The number of test case data points N that must be checked is given by

$$N = n^2 \times fpts \times Kpts \times Tpts \tag{64}$$

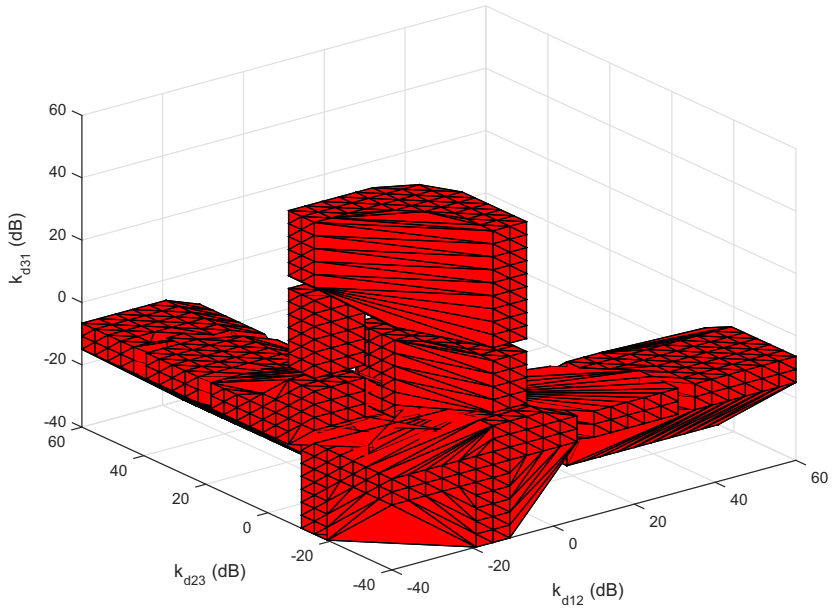

Figure 24: Disallowed damping values with $T_d = 0.0$ ms, three-area system.

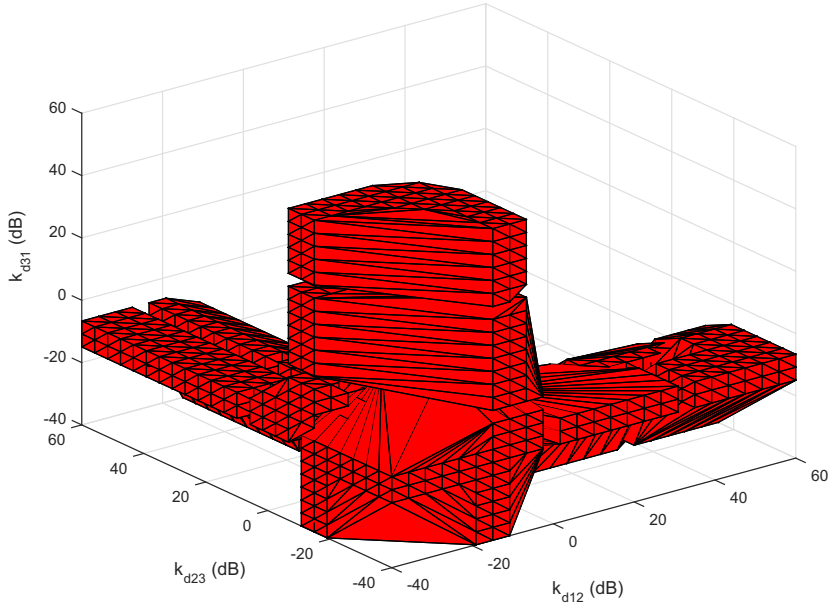

Figure 25: Disallowed damping values with $T_d = 1.0$ ms, three-area system.

where n is the size of the A matrix, $fpts$ is the number of frequency points, $Kpts$ is the number of gain values tested (assuming same gain at all controllers), and $Tpts$ is the number of time delay values of

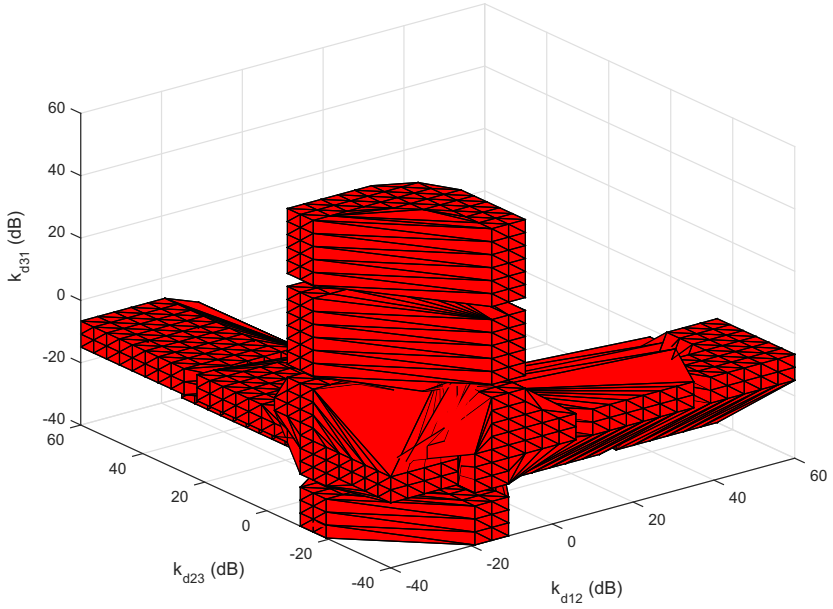

Figure 26: Disallowed damping values with $T_d = 10$ ms, three-area system.

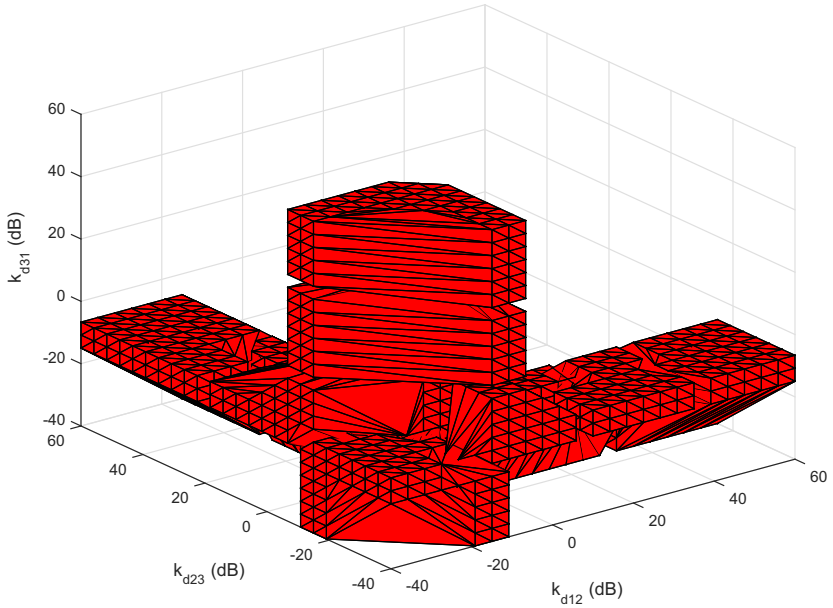

Figure 27: Disallowed damping values with $T_d = 100$ ms, three-area system.

interest. If each controller is tested for a unique gain value, the number of test cases increases to

$$N = n^2 \times fpts \times Kpts^{NC} \times Tpts \tag{65}$$

where NC is the number of control systems with independent gain settings. For minni-WECC system with 34 generators, a test of 10 possible gain values results in 10^{34} potential cases. Therefore, for large power systems, it is only feasible to test for constant gain values. This is somewhat reasonable, given that frequency droop is typically set at 5%. The next section presents results for the nominal minni-WECC linearized model.

3.5.2 Minni-WECC Nominal Case

In order to examine the stability for the entire minni-WECC there are two possible uses for the method outlined above. In order to use the method as a design tool, some constrains on the allowable values of k_d must be imposed. This can be as simple as selecting a single k_d for all the generators, or applying a weighting for each generator. This will reduce the parameter space down to a single variable that can be easily automated to find stable values. By using the method as a validation tool, we can select damping gains through some other strategy and determine the degree of stability of the resulting system.

As shown in Figures 28 and 29 the method determines the stability of a solution by checking to see if the Nyquist contour crosses into the ESAC boundary. In order to reduce the computational complexity of the model, a single k_d was chosen and used to build a controller $\mathbf{K}$. The damping coefficient was then varied from -40 dB to 40 dB for each time delay. A visualization of the results, where 1 represents a stable result and 0 represents an unstable result, for a 10 ms time delay is shown in Figure 30. The results for a 100 ms time delay are shown in Figure 31. From this result it can be seen that k_d less than -10 dB ($k_d < 0.3162$) is always stable for this case. While some k_d values greater than this value result in stable Nyquist plots, other concerns will eliminate these potential values. Repeating this code for T_d also show that k_d less than -10 dB will result in stable Nyquist contours. To apply this technique to a generic system, the following steps should be applied:

1. obtain a linearized state space model about an operating point.
2. define the feedback structure and signals with communications delays.
3. apply the ESAC criterion to transfer functions of interest for the expected range of gain and time delay values.
4. “acceptable” gain and time delay values pass the ESAC criterion for all transfer functions of interest.

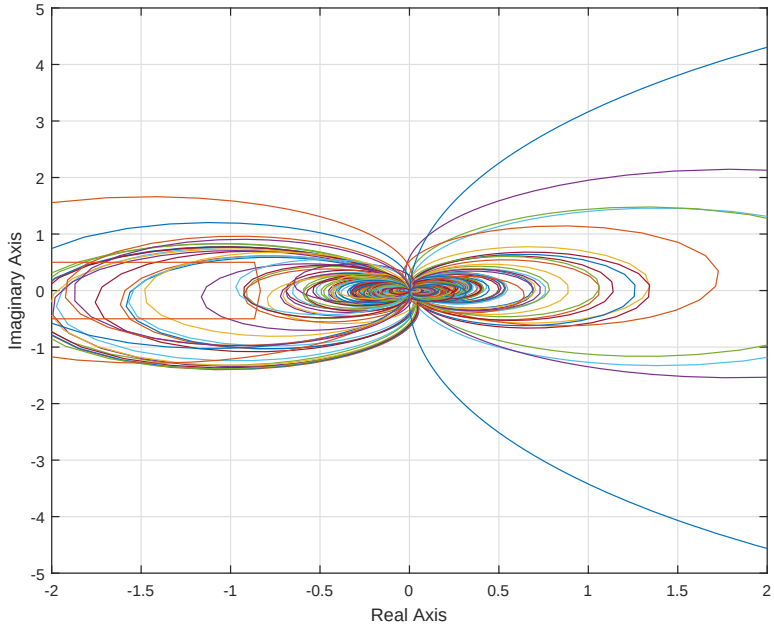

Figure 28: Unstable Nyquist curves $k_d = 0.4132$ and $T_d = 0.012$ ms.

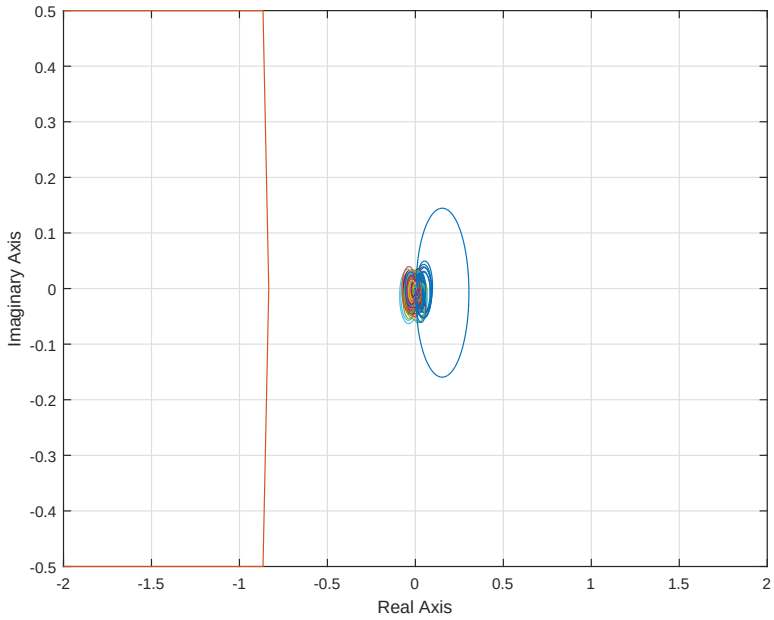

Figure 29: Stable Nyquist curves $k_d = 0.01$ and $T_d = 0.120$ ms.

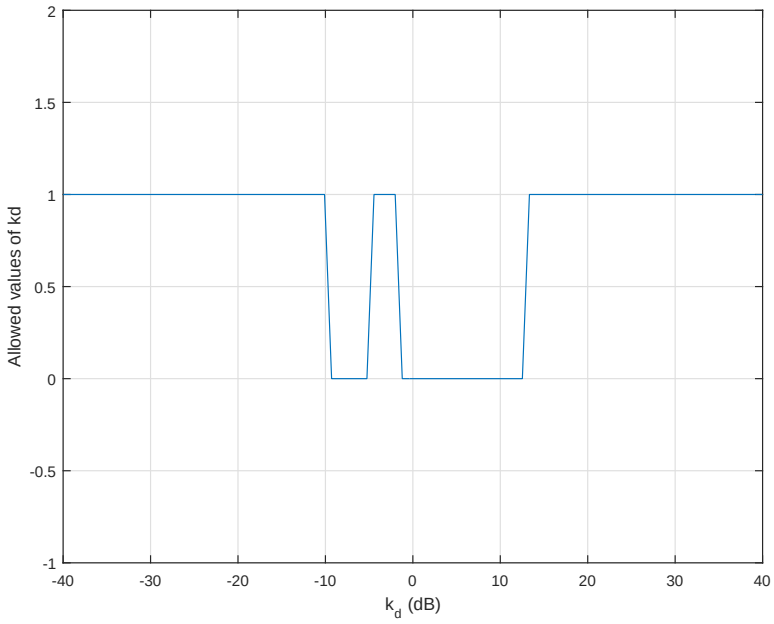

Figure 30: Allowable k_d values with $T_d = 10$ ms, minni-WECC model.

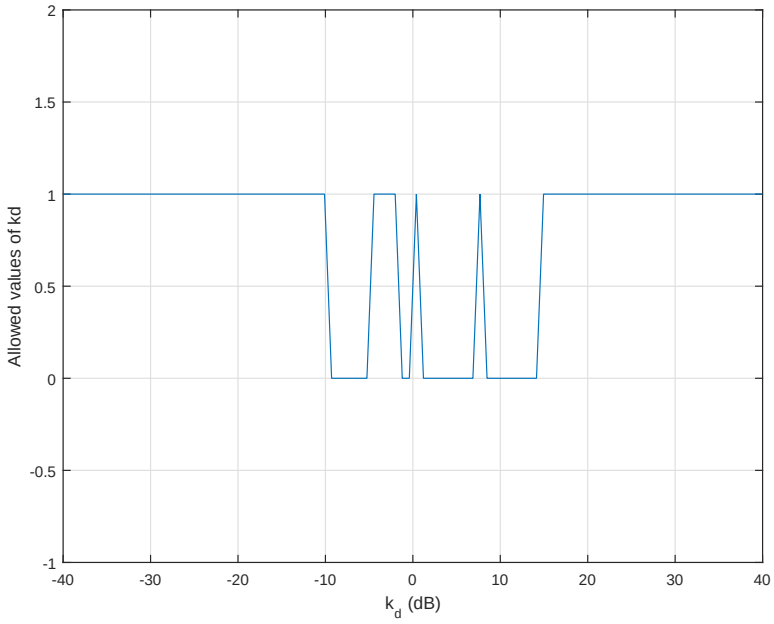

Figure 31: Allowable k_d values with $T_d = 100$ ms, minni-WECC model.

3.6 Vector Lyapunov Methods

Vector Lyapunov methods are well suited to evaluate the stability of control algorithms with structured perturbations. These perturbations may be used to address model or communications uncertainty. These methods are also a powerful analysis tool for the evaluation of distributed control strategies with uncertain communications. To apply these methods, the system model must be partitioned into N interconnected subsystems such that

$$\boldsymbol{S}: \quad \dot{x}_i = A_i x_i + \sum_{j=1}^{N} e_{ij} A_{ij} x_j, \quad i \in \boldsymbol{N} \tag{66}$$

A_i and A_{ij} are assumed to be constant matrices, and each subsystem A_i is assumed to be stable (the stability may be the result of local feedback applied to an unstable system). The dynamics of the i^{th} subsystem are modeled by

$$\boldsymbol{S}_i: \quad \dot{x}_i = A_i x_i \tag{67}$$

Note that for this formulation, there are no overlapping states in the subsystems. For each subsystem, states from other subsystems only interact through the coupling parameter e_{ij}. For an $e_{ij} = 1$, the system is connectively stable for $e_{ij} \in [0, 1]$ if the stability criteria are met. Thus, subsystem model uncertainties can be captured by the A_{ii} matrix, and communication uncertainty with feedback from other subsystems is captured by the A_{ij} matrix. For cases with no interconnection, $e_{ij} = 0$.

For the system to be collectively stable [13], the test matrix $W = (w_{ij})$ defined in equation (68) must be an $\mathcal{M}$ matrix.

$$w_{ij} = \begin{cases} i = j, & \frac{\lambda_m(G_i)}{2\lambda_M(H_i)} - \bar{e}_{ii}\lambda_M^{1/2}(A_{ii}^T A_{ii}) \\ i \neq j, & -\bar{e}_{ij}\lambda_M^{1/2}(A_{ij}^T A_{ij}) \end{cases} \tag{68}$$

$\lambda_m(\bullet)$ is defined as the minimum eigenvalue, while $\lambda_M(\bullet)$ is defined as the maximum eigenvalue. Furthermore, the matrices H_i and G_i satisfy the Lyapunov matrix equation

$$A_i^T H_i + H_i A_i + G_i = 0 \tag{69}$$

A simple test to determine if W is an $\mathcal{M}$ matrix is that every real eigenvalue of W is positive. Forty conditions equivalent to the statement "W is a nonsingular $\mathcal{M}$ matrix" are found in [30]. The smaller the off diagonal elements w_{ij} of W relative to the diagonal elements, the likelihood of W being an $\mathcal{M}$ matrix increases [13]. Therefore, a goal should be to maximize the following ratio

$$\text{Find: } \max_{G_i} \frac{\lambda_m(G_i)}{\lambda_M(H_i)} \tag{70}$$

In [13], it is shown that selecting G_i as the identity matrix maximizes the ratio above. This yields a simplified test matrix W:

$$w_{ij} = \begin{cases} i = j, & \frac{1}{2\lambda_M(H_i)} - \bar{e}_{ii}\lambda_M^{1/2}(A_{ii}^T A_{ii}) \\ i \neq j, & -\bar{e}_{ij}\lambda_M^{1/2}(A_{ij}^T A_{ij}) \end{cases} \tag{71}$$

The next section presents results for a two-area power system model.

Table 4: Two-Area System Model Quantities

Quantity	Description
M_i	Area i inertia
D_i	Area i damping
T	Synchronizing torque coefficient
ΔP_{Li}	Area i load variation
ΔP_{Di}	Area i damping torque
$\Delta\omega_i$	Area i change in speed
$\Delta\delta_i$	Area i change in angle

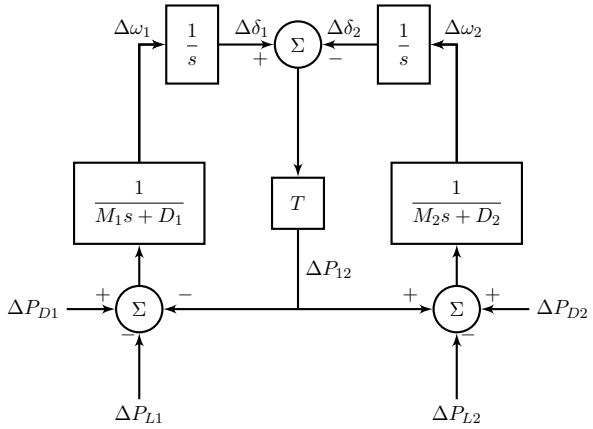

Figure 32: Two-area system [31] with damping control.

3.6.1 Two-Area System

A critical step in applying distributed control concepts is the partition of the system. In this section, we consider a 2-area power system model, illustrated in Figure 32. The parameters are defined in Table 4. Different PV penetrations can be approximated by adjusting the inertia and damping based on the generation characteristics. The two-area model simplifies to the following state space system.

$$\dot{\boldsymbol{x}} = A\boldsymbol{x} + B\boldsymbol{u} \tag{72}$$

$$\boldsymbol{y} = C\boldsymbol{x} \tag{73}$$

where

$$\boldsymbol{x} = \begin{bmatrix} \Delta\omega_1 \\ \Delta\delta_1 \\ \Delta\omega_2 \\ \Delta\delta_2 \end{bmatrix}, \quad \boldsymbol{u} = \begin{bmatrix} \Delta P_{D1} \\ \Delta P_{D2} \end{bmatrix}, \tag{74}$$

$$A = \begin{bmatrix} -\frac{D_1}{M_1} & -\frac{T}{M_1} & 0 & \frac{T}{M_1} \\ 1 & 0 & 0 & 0 \\ 0 & \frac{T}{M_2} & -\frac{D_2}{M_2} & -\frac{T}{M_2} \\ 0 & 0 & 1 & 0 \end{bmatrix}, \tag{75}$$

$$B = \begin{bmatrix} \frac{1}{M_1} & 0 \\ 0 & 0 \\ 0 & \frac{1}{M_2} \\ 0 & 0 \end{bmatrix}, \quad C = \begin{bmatrix} 1 & 0 & 0 & 0 \\ 0 & 1 & 0 & 0 \\ 0 & 0 & 1 & 0 \\ 0 & 0 & 0 & 1 \end{bmatrix}. \tag{76}$$

We assume that each state is observable, e.g., bus frequency and angle data are available for Phasor Measurement Unit (PMU) data. The system model can be rearranged into two loosely coupled systems, as shown by the partitions below.

$$A = \left[\begin{array}{cc|cc} -\frac{D_1}{M_1} & -\frac{T}{M_1} & 0 & \frac{T}{M_1} \\ 1 & 0 & 0 & 0 \\ \hline 0 & \frac{T}{M_2} & -\frac{D_2}{M_2} & -\frac{T}{M_2} \\ 0 & 0 & 1 & 0 \end{array}\right] \tag{77}$$

$$B = \left[\begin{array}{c|c} \frac{1}{M_1} & 0 \\ 0 & 0 \\ \hline 0 & \frac{1}{M_2} \\ 0 & 0 \end{array}\right] \tag{78}$$

Since the stiffness of the transmission system coupling the two areas can change over time, we introduce a coupling coefficient $e \in [0, 1]$. The two area system can be decomposed along the dashed lines to obtain the system in equations 84-85. This is equivalent to the interconnection of two subsystems

$$\boldsymbol{S}_1: \qquad \dot{x}_1 = \begin{bmatrix} -\frac{D_1}{M_1} & -\frac{T}{M_1} \\ 1 & 0 \end{bmatrix} x_1 + \begin{bmatrix} \frac{1}{M_1} \\ 0 \end{bmatrix} u_1 \tag{79}$$

$$\boldsymbol{S}_2: \qquad \dot{x}_2 = \begin{bmatrix} -\frac{D_2}{M_2} & -\frac{T}{M_2} \\ 1 & 0 \end{bmatrix} x_2 + \begin{bmatrix} \frac{1}{M_2} \\ 0 \end{bmatrix} u_2 \tag{80}$$

where $x_1 = (\Delta\omega_1, \Delta\delta_1)^T$ and $x_2 = (\Delta\omega_2, \Delta\delta_2)^T$ are the states of the two subsystems. The goal is for the two subsystems to be stable when decoupled ($e = 0$) using the decentralized feedback laws

$$\Delta P_{D1} = -k_1 x_1, \quad \Delta P_{D2} = -k_2 x_2, \tag{81}$$

The feedback gains, $k_i = (k_{i1}, k_{i2})$, are selected so that the closed-loop subsystems are stable.

$$\hat{\boldsymbol{S}}_1: \qquad \dot{x}_1 = \begin{bmatrix} -\frac{D_1}{M_1} - \frac{k_{11}}{M_1} & -\frac{T}{M_1} - \frac{k_{12}}{M_1} \\ 1 & 0 \end{bmatrix} x_1 \tag{82}$$

$$\hat{\boldsymbol{S}}_2: \qquad \dot{x}_2 = \begin{bmatrix} -\frac{D_2}{M_2} - \frac{k_{21}}{M_2} & -\frac{T}{M_2} - \frac{k_{22}}{M_2} \\ 1 & 0 \end{bmatrix} x_2 \tag{83}$$

The overall system model is described by

$$\begin{bmatrix} \dot{\Delta\omega_1} \\ \dot{\Delta\delta_1} \end{bmatrix} = \begin{bmatrix} -\frac{D_1}{M_1} & -\frac{T}{M_1} \\ 1 & 0 \end{bmatrix} \begin{bmatrix} \Delta\omega_1 \\ \Delta\delta_1 \end{bmatrix} + \begin{bmatrix} \frac{1}{M_1} \\ 0 \end{bmatrix} \Delta P_{D1} + e \begin{bmatrix} 0 & \frac{T}{M_1} \\ 0 & 0 \end{bmatrix} \begin{bmatrix} \Delta\omega_2 \\ \Delta\delta_2 \end{bmatrix} \tag{84}$$

$$\begin{bmatrix} \Delta\dot{\omega}_2 \\ \Delta\dot{\delta}_2 \end{bmatrix} = \begin{bmatrix} -\frac{D_2}{M_2} & -\frac{T}{M_2} \\ 1 & 0 \end{bmatrix} \begin{bmatrix} \Delta\omega_2 \\ \Delta\delta_2 \end{bmatrix} + \begin{bmatrix} \frac{1}{M_2} \\ 0 \end{bmatrix} \Delta P_{D2} + e \begin{bmatrix} 0 & \frac{T}{M_2} \\ 0 & 0 \end{bmatrix} \begin{bmatrix} \Delta\omega_1 \\ \Delta\delta_1 \end{bmatrix} \tag{85}$$

Note that for this model, there are no communications uncertainty, just uncertainty in the interconnection strength T/M_i. This case only considers local feedback. Results for this system are shown in Figure 33. The system is connectively stable for a range of gains when $k11$ is approximately equal to $k12$. Note that it is not connectively stable without feedback ($k = 0$ case).

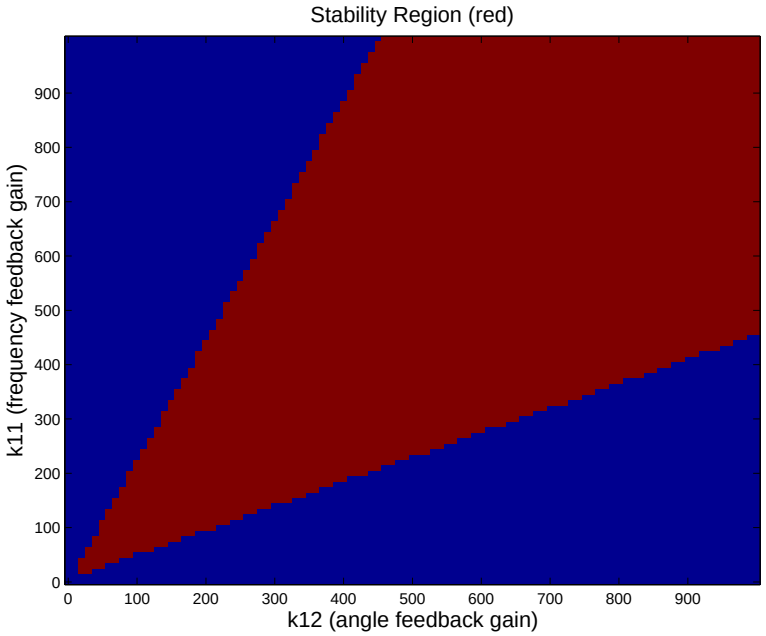

Figure 33: Two-area system stability region, T=3, $M1$=8, $M2$=8, $D2$=1. Local feedback, no communications uncertainty.

The next case considered looks at limited local communications bandwidth and uncertainty in the coupling between areas. Communications bandwidth limitations are modeled by a first order low-pass filter

$$\frac{x^f(s)}{x(s)} = \frac{1}{s\tau + 1} \tag{86}$$

The resulting models for the two subsystems are given by

$$\begin{bmatrix} \Delta\dot{\omega}_1 \\ \Delta\dot{\delta}_1 \\ \Delta\dot{\omega}_1^f \\ \Delta\dot{\delta}_1^f \end{bmatrix} = \begin{bmatrix} -\frac{D_1}{M_1} & -\frac{T}{M_1} & -\frac{k_{11}}{M_1} & -\frac{k_{12}}{M_1} \\ 1 & 0 & 0 & 0 \\ \frac{1}{\tau} & 0 & -\frac{1}{\tau} & 0 \\ 0 & \frac{1}{\tau} & 0 & -\frac{1}{\tau} \end{bmatrix} \begin{bmatrix} \Delta\omega_1 \\ \Delta\delta_1 \\ \Delta\omega_1^f \\ \Delta\delta_1^f \end{bmatrix} + e \begin{bmatrix} 0 & \frac{T}{M_1} & 0 & 0 \\ 0 & 0 & 0 & 0 \\ 0 & 0 & 0 & 0 \\ 0 & 0 & 0 & 0 \end{bmatrix} \begin{bmatrix} \Delta\omega_2 \\ \Delta\delta_2 \\ \Delta\omega_2^f \\ \Delta\delta_2^f \end{bmatrix} \tag{87}$$

$$\begin{bmatrix} \Delta\dot{\omega}_2 \\ \Delta\dot{\delta}_2 \\ \Delta\dot{\omega}_2^f \\ \Delta\dot{\delta}_2^f \end{bmatrix} = \begin{bmatrix} -\frac{D_2}{M_2} & -\frac{T}{M_2} & -\frac{k_{11}}{M_2} & -\frac{k_{12}}{M_2} \\ 1 & 0 & 0 & 0 \\ \frac{1}{\tau} & 0 & -\frac{1}{\tau} & 0 \\ 0 & \frac{1}{\tau} & 0 & -\frac{1}{\tau} \end{bmatrix} \begin{bmatrix} \Delta\omega_2 \\ \Delta\delta_2 \\ \Delta\omega_2^f \\ \Delta\delta_2^f \end{bmatrix} + e \begin{bmatrix} 0 & \frac{T}{M_2} & 0 & 0 \\ 0 & 0 & 0 & 0 \\ 0 & 0 & 0 & 0 \\ 0 & 0 & 0 & 0 \end{bmatrix} \begin{bmatrix} \Delta\omega_1 \\ \Delta\delta_1 \\ \Delta\omega_1^f \\ \Delta\delta_1^f \end{bmatrix} \tag{88}$$

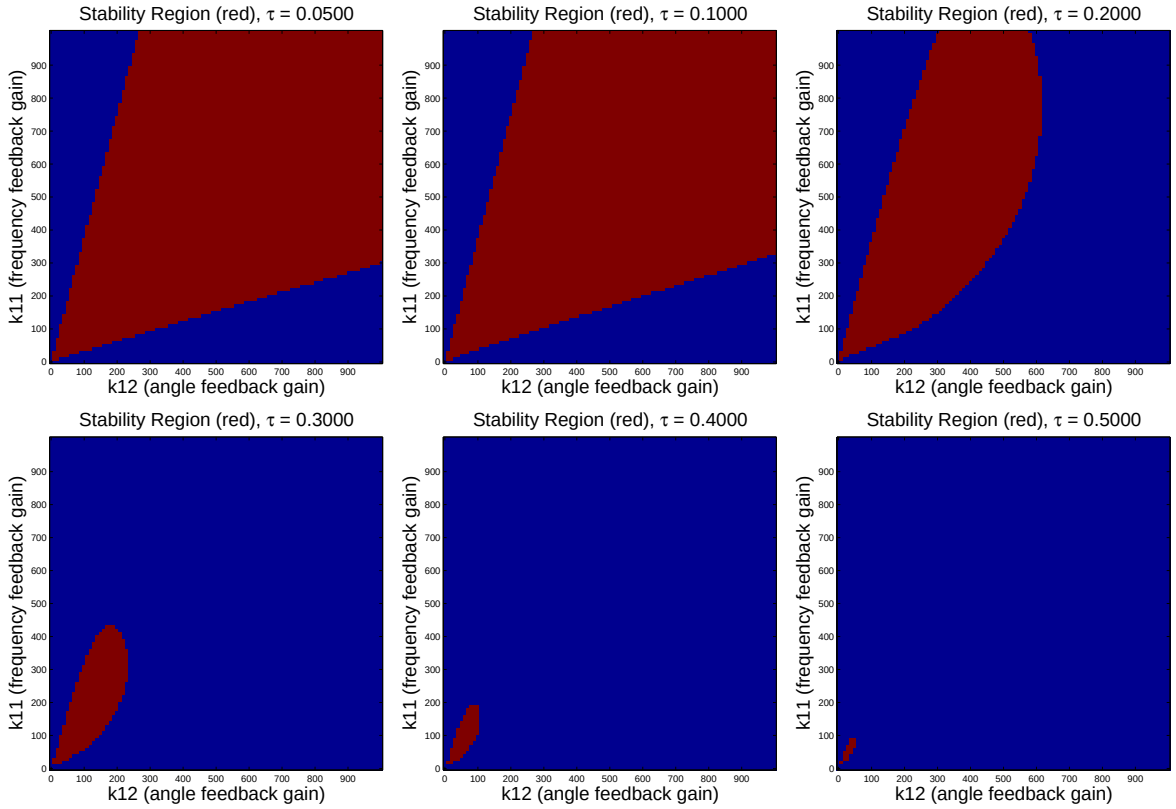

Figure 34: Two-area system results for bandwidth limited local communications and uncertainty in interconnection strength.

Results for the case of limited bandwidth local communications are summarized in Figure 34. As the bandwidth of the local feedback signal is reduced, the stability region is reduced.

Next, we considered the case of limited global communications bandwidth and no limits on local feedback, as well as uncertainty in the interconnection strength T. The models for this case are shown below. The local feedback is defined by k_{ilocal} while the global feedback is defined as k_{ij}. Results for this case are summarized in Figure 35. For this case, as small amount of delay on the global feedback actually increases the range of acceptable gain values.

$$\begin{bmatrix} \dot{\Delta\omega_1} \\ \dot{\Delta\delta_1} \\ \dot{\Delta\omega_1^f} \\ \dot{\Delta\delta_1^f} \end{bmatrix} = \begin{bmatrix} -\frac{D_1+k_{1local}}{M_1} & -\frac{T+k_{2local}}{M_1} & 0 & 0 \\ 1 & 0 & 0 & 0 \\ \frac{1}{\tau} & 0 & -\frac{1}{\tau} & 0 \\ 0 & \frac{1}{\tau} & 0 & -\frac{1}{\tau} \end{bmatrix} \begin{bmatrix} \Delta\omega_1 \\ \Delta\delta_1 \\ \Delta\omega_1^f \\ \Delta\delta_1^f \end{bmatrix} + e \begin{bmatrix} 0 & \frac{T}{M_1} & \frac{k_{11}}{M_1} & \frac{k_{12}}{M_1} \\ 0 & 0 & 0 & 0 \\ 0 & 0 & 0 & 0 \\ 0 & 0 & 0 & 0 \end{bmatrix} \begin{bmatrix} \Delta\omega_2 \\ \Delta\delta_2 \\ \Delta\omega_2^f \\ \Delta\delta_2^f \end{bmatrix} \quad (89)$$

$$\begin{bmatrix} \dot{\Delta\omega_2} \\ \dot{\Delta\delta_2} \\ \dot{\Delta\omega_2^f} \\ \dot{\Delta\delta_2^f} \end{bmatrix} = \begin{bmatrix} -\frac{D_2+K_{1local}}{M_2} & -\frac{T+k_{2local}}{M_2} & 0 & 0 \\ 1 & 0 & 0 & 0 \\ \frac{1}{\tau} & 0 & -\frac{1}{\tau} & 0 \\ 0 & \frac{1}{\tau} & 0 & -\frac{1}{\tau} \end{bmatrix} \begin{bmatrix} \Delta\omega_2 \\ \Delta\delta_2 \\ \Delta\omega_2^f \\ \Delta\delta_2^f \end{bmatrix} + e \begin{bmatrix} 0 & \frac{T}{M_2} & \frac{k_{11}}{M2} & \frac{k_{12}}{M2} \\ 0 & 0 & 0 & 0 \\ 0 & 0 & 0 & 0 \\ 0 & 0 & 0 & 0 \end{bmatrix} \begin{bmatrix} \Delta\omega_1 \\ \Delta\delta_1 \\ \Delta\omega_1^f \\ \Delta\delta_1^f \end{bmatrix} \quad (90)$$

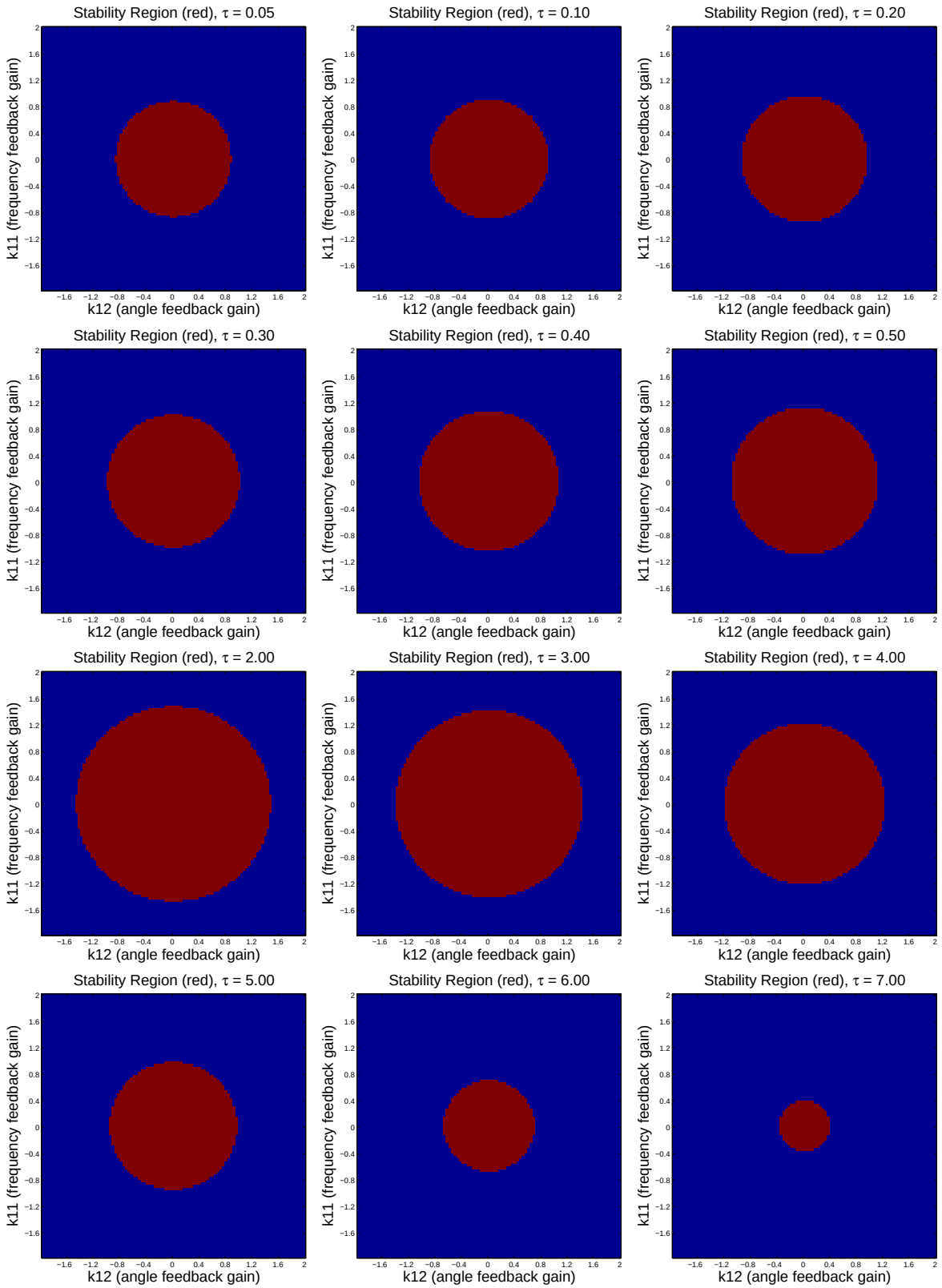

Figure 35: Two-area system, case of limited bandwidth global communications, unlimited local communications, and uncertainty in the interconnection strength.

3.7 Hamiltonian Surface shaping and Power Flow Control (HSSPFC)

Our goal in developing a nonlinear control design methodology is to help address some of the key issues surrounding high penetration of renewable energy (wind, solar) generation for the future smart grid. A simple example is explored further to show the necessary power and energy storage requirements.

The HSSPFC design [32] steps are summarized in the following ten steps: 1) define Reduced Order Model (ROM), 2) formulate the kinetic and potential energies, 3) formulate the Hamiltonian, 4) derive the power flow (Hamiltonian rate), 5) design the nonlinear control laws, 6) determine the static stability conditions, 7) determine the dynamic stability conditions, 8) optimize the control system (controller gains) for the desired performance, 9) perform enterprising optimization (specific to Microgrid mission metrics), and 10) simultaneously minimize information flow and energy storage. The following section investigates the HSSPFC design, analysis and numerical simulations as applied to a conventional One Machine Infinite Bus (OMIB) model with variable input that represents stochastic solar generation to determine stability and performance via energy storage systems. The next section develops the HSSPFC for simple AC grid systems and demonstrates the reduced order model to initial conditions offsets for the spinning machines.

3.7.1 Example 1: OMIB model and control

Summarizing and starting with a power engineering OMIB model from RNM conventions [33], [34], [35] that best reflects the new nonlinear power flow control methodology gives

$$T_m - T_e = J\dot{\omega}_{RM} + B\omega_{RM} \tag{91}$$

$$\omega_{RM} = \omega/(N_p/2) \;\; \omega = \omega_{ref} + \dot{\delta} \tag{92}$$

$$T_m - T_e = \hat{J}(\dot{\omega}_{ref} + \ddot{\delta}) + \hat{B}(\omega_{ref} + \dot{\delta}) \tag{93}$$

Initially, the Hamiltonian is defined as

$$\mathcal{H} = \frac{1}{2}\hat{J}\omega^2 \tag{94}$$

where the power flow or Hamiltonian rate becomes

$$\dot{\mathcal{H}} = \hat{J}\dot{\omega}\omega = P_m - P_e - \hat{B}\omega^2. \tag{95}$$

The next step is to add the approximate power flows from the generator, mechanical controls, and unified power control (UPFC) [33] [1] as

$$\begin{array}{rcl} u_{e_1} & = & K_{P_e}\cos\delta_s + K_{D_e}\sin\delta\dot{\delta} + K_{I_e}\sin\delta\int_0^t(\delta-\delta_s)d\tau \\ u_{e_2} & = & K_{P_e}\sin\delta_s + K_{D_e}\cos\delta\dot{\delta} - K_{I_e}\cos\delta\int_0^t(\delta-\delta_s)d\tau. \end{array} \tag{96}$$

Finally, substitute these control laws into the previous equation and simplifying yields the following

$$\hat{J}\ddot{\delta} + [P_{e_c}\sin\delta - P_{m_c}] + P_{e_c}K_{P_e}\sin(\delta-\delta_s) = -[\hat{B} + P_{e_c}K_{D_e}]\dot{\delta} - K_{I_e}\int_0^t(\delta-\delta_s)d\tau. \tag{97}$$

The static stability condition becomes

$$\mathcal{H} = \frac{1}{2}\hat{J}\dot{\delta}^2 + P_{e_c}(1+K_{P_e})(1-\cos(\delta-\delta_s)) \tag{98}$$

with $\mathcal{H}$ being positive definite and the set point determined as

$$\delta_s = \sin^{-1}(P_{m_c}/P_{e_c}). \tag{99}$$

The dynamic stability condition for a passively stable control design yields

$$\oint_{\tau}[\hat{B}+P_{e_c}K_{D_e}]\dot{\delta}^2dt > -\oint_{\tau}[P_{e_c}K_{I_e}\int_0^t(\delta-\delta_s)d\tau_1]\dot{\delta}dt. \tag{100}$$

Clearly, the nonlinear PID controller through the proportional term expands the region of stability by increasing the Potential Energy Boundary Surface (PEBS) from

$$P_{e_c} \quad \rightarrow \quad P_{e_c}(1+K_{P_e}) \tag{101}$$

and by adding the PID controller integrator and derivative terms, the system will be able to respond more quickly, increasing the performance, and reducing the transient settling response times. A feedforward control term can be added to the UPFC controllers and is defined by

$$\begin{array}{rcl} u_{e_1} & = & u_{e_1}-[(P_{m_{ref}}-P_m(t))/P_{max}]\sin\delta \\ u_{e_2} & = & u_{e_2}-[(P_{m_{ref}}-P_m(t))/P_{max}]\cos\delta \end{array} \tag{102}$$

where $P_{m_{ref}}$ is designed to emulate a constant input and $P_m(t)$ is from variable generation such as solar power generation.

3.7.2 UPFC Control Simulation

Initially, the OMIB without the UPFC is given a faulted initial condition that is away from the stable equilibrium point and the machine goes unstable (see Figure 36 left). By adding the UPFC proportional gain (energy storage) the machine becomes stable (see Figure 36 right) and returns to the equilibrium set point. The UPFC control system gains are designed to ensure static stability and dynamic stability

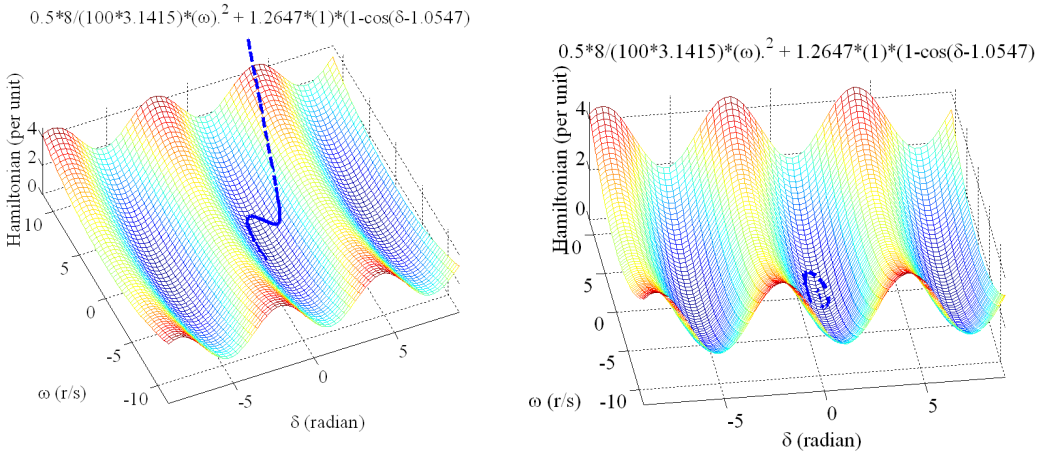

Figure 36: Unstable without UPFC (left) and stable with UPFC (right) (see [35]).

conditions and were adjusted for tolerable transient responses. The dynamic stability performance is determined with Integral and Derivative terms of the nonlinear PID UPFC control law. Figure 37 (left) shows the phase plane plot and Figure 37 (right) the transient response. The stochastic nature of the solar input is approximated very simply as a random input as shown in Figure 38. The feed-forward component is used to help predict the random process and helps to give the desired constant power reference input. Figure 39 (left) and (right), respectively, show the corresponding phase plane and transient responses, respectively.

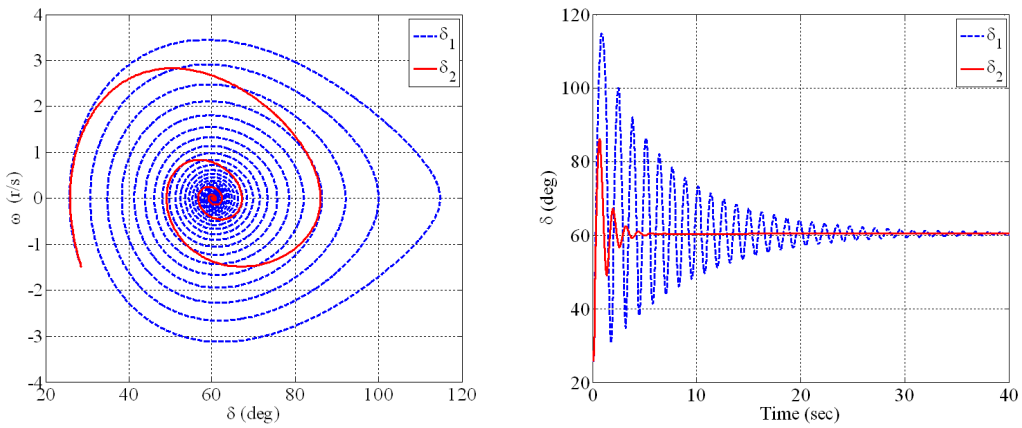

Figure 37: Dynamic stability and performance (left) and transient response (right) (see [35]).

To achieve the constant power input to the grid for the OMIB the UPFC provides both the additional power and energy storage to the system. This design and analysis allows one to determine the required energy storage and power requirements as shown in Figure 40. Figure 40 (left) is for the UPFC design without feedforward and Figure 40 (right) is the UPFC design with feedforward. These transient responses can be used to size critical components in the system by providing peak power, energy storage amounts (charge/discharge profiles), and device bandwidths for necessary power electronics as required to achieve the given performance specifications.

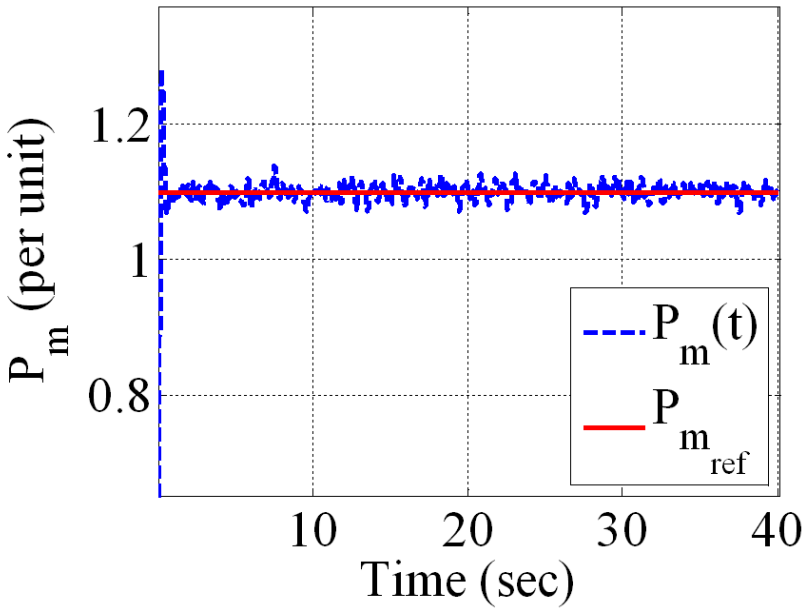

Figure 38: Constant power signal compared to stochastic or random signal input (see [35]).

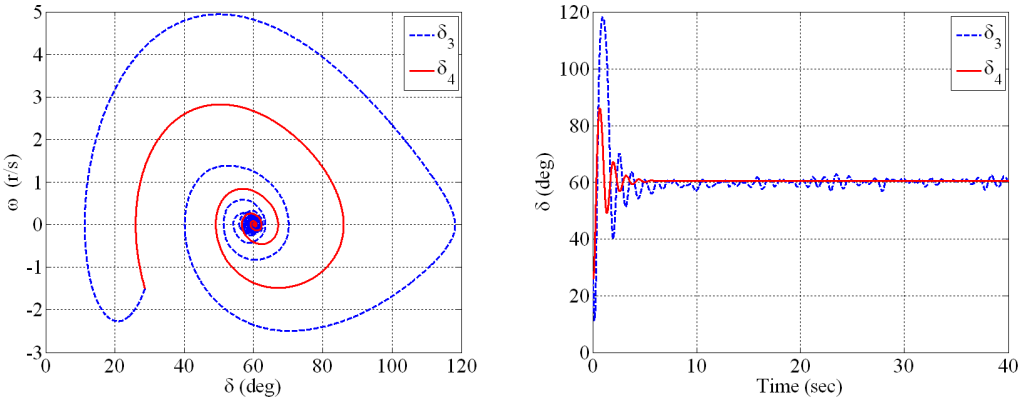

Figure 39: Variable generation dynamic stability and performance (left) and transient response (right) (see [35]).

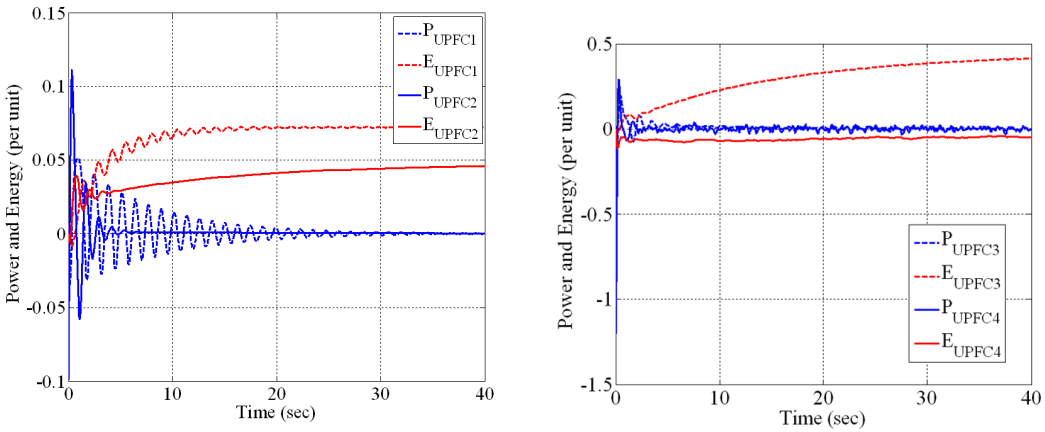

Figure 40: Baseline UPFC energy storage (red) and power (blue) transients (left) and UPFC with feedforward energy storage (red) and power (blue) transients (right) (see [35]).

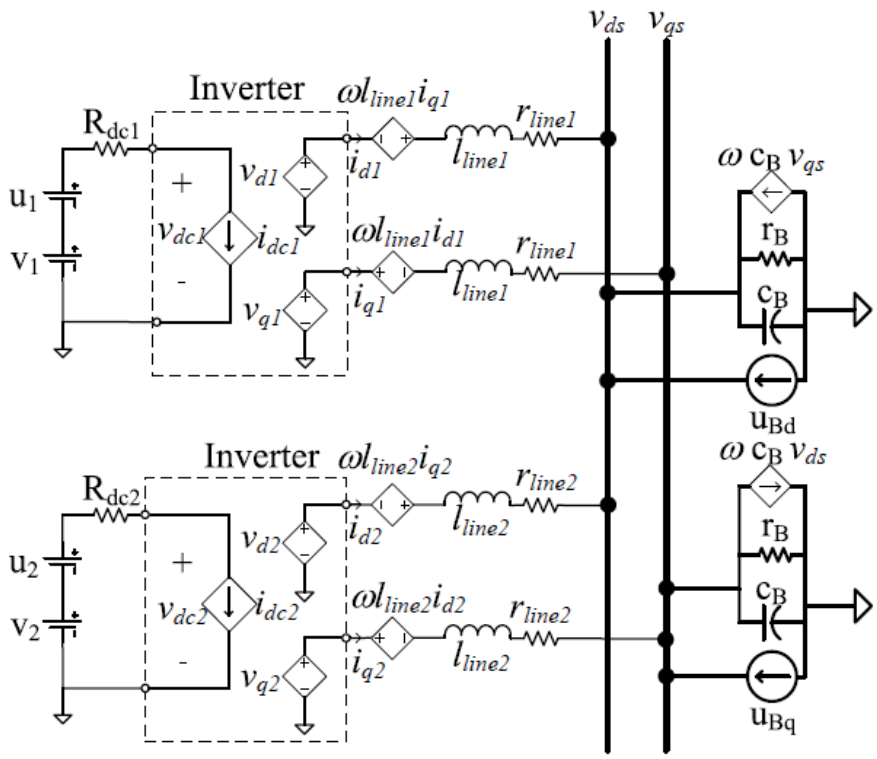

Figure 41: AC inverter model with two generation inputs and load and bus storage components attached to AC bus (see [36]).

3.7.3 Simple AC Inverter Electric Grid Systems

The goal of this section is to identify reduced order models for control designs and establish stability and performance criteria for AC inverter electric grid systems that have both spinning machines and AC inverters that support renewable energy generation sources such as PV. Preliminary development for inverter based AC electric grid models has been documented in reference [36] and the schematic shown in Figure 41. The model can be summarized in marix form as

$$\mathbf{M}\dot{\mathbf{x}} = \mathbf{R}\mathbf{x} + \mathbf{D}\mathbf{u} + \mathbf{B}\mathbf{v} = [\bar{\mathbf{R}} + \tilde{\mathbf{R}}] + \mathbf{D}\mathbf{u} + \mathbf{B}\mathbf{v} \tag{103}$$

where

$$\begin{array}{rcc} \mathbf{x} & = & [i_{d_1}, i_{q_1}, i_{d_2}, i_{q_2}, v_{d_b}, v_{q_b}]^T \\ \mathbf{u} & = & [u_1, u_2, u_{d_b}, u_{q_b}]^T \\ \mathbf{v} & = & [v_1, v_2]^T \end{array} \tag{104}$$

and the matricies are defined as

$$\mathbf{M} = \begin{bmatrix} L_1 & 0 & 0 & 0 & 0 & 0 \\ 0 & L_1 & 0 & 0 & 0 & 0 \\ 0 & 0 & L_2 & 0 & 0 & 0 \\ 0 & 0 & 0 & L_2 & 0 & 0 \\ 0 & 0 & 0 & 0 & C_B & 0 \\ 0 & 0 & 0 & 0 & 0 & C_B \end{bmatrix} \tag{105}$$

$$\mathbf{R} = \begin{bmatrix} -R_1 & \omega L_1 & 0 & 0 & -1 & 0 \\ -\omega L_1 & -R_1 & 0 & 0 & 0 & -1 \\ 0 & 0 & -R_2 & \omega L_2 & -1 & 0 \\ 0 & 0 & -\omega L_2 & -R_2 & 0 & -1 \\ 1 & 0 & 1 & 0 & -\frac{1}{R_b} & \omega C_b \\ 0 & 1 & 0 & 1 & -\omega C_b & -\frac{1}{R_b} \end{bmatrix} \tag{106}$$

$$\mathbf{B} = \begin{bmatrix} \frac{1}{2}\sqrt{\frac{3}{2}}(\cos\phi_1)\lambda_1 & 0 & 0 & 0 \\ \frac{1}{2}\sqrt{\frac{3}{2}}(\sin\phi_1)\lambda_1 & 0 & 0 & 0 \\ 0 & \frac{1}{2}\sqrt{\frac{3}{2}}(\cos\phi_2)\lambda_2 & 0 & 0 \\ 0 & \frac{1}{2}\sqrt{\frac{3}{2}}(\sin\phi_2)\lambda_2 & 0 & 0 \\ 0 & 0 & 1 & 0 \\ 0 & 0 & 0 & 1 \end{bmatrix} \tag{107}$$

and

$$\mathbf{D} = \begin{bmatrix} \frac{1}{2}\sqrt{\frac{3}{2}}(\cos\phi_1)\lambda_1 & 0 \\ \frac{1}{2}\sqrt{\frac{3}{2}}(\sin\phi_1)\lambda_1 & 0 \\ 0 & \frac{1}{2}\sqrt{\frac{3}{2}}(\cos\phi_2)\lambda_2 \\ 0 & \frac{1}{2}\sqrt{\frac{3}{2}}(\sin\phi_2)\lambda_2 \\ 0 & 0 \\ 0 & 0 \end{bmatrix}. \tag{108}$$

To illustrate the control system design, define the error state along with the reference control as

$$\mathbf{e} = \tilde{\mathbf{x}} = \mathbf{x_{ref}} - \mathbf{x}$$

$$\mathbf{M}\dot{\mathbf{x}}_{\mathbf{ref}} = \mathbf{R}\mathbf{x_{ref}} + \mathbf{B}\mathbf{v} + \mathbf{D}\mathbf{u_{ref}}. \tag{109}$$

It is assumed that the reference state vector is constant and operating at some desired steady-state condition, and the reference control signal becomes

$$\mathbf{D}\mathbf{u_{ref}} = -\mathbf{R}\mathbf{x_{ref}} - \mathbf{B}\mathbf{v}. \tag{110}$$

Next, based on the error-state the Hamiltonian or energy surface is defined as

$$\mathcal{H} = \frac{1}{2}\tilde{\mathbf{x}}^T\mathbf{M}\tilde{\mathbf{x}} + \frac{1}{2}(\int \tilde{\mathbf{x}}dt)^T\mathbf{K_I}(\int \tilde{\mathbf{x}}dt) \;\; \tilde{\mathbf{x}} = \mathbf{0} \tag{111}$$

where the controller integral term provides a control potential energy to help design or shape the energy surface to meet the **static stability condition**. Note the integral controller diagonal gain matrix is positive definite.

The Hamiltonian time derivative (or power flow) becomes

$$\dot{\mathcal{H}} = \tilde{\mathbf{x}}^T\mathbf{M}\dot{\tilde{\mathbf{x}}} = \tilde{\mathbf{x}}^{\mathbf{T}}[\mathbf{M}\dot{\mathbf{x}}_{\mathbf{ref}} - \mathbf{M}\dot{\mathbf{x}}] + \tilde{\mathbf{x}}\mathbf{K_I}\int \tilde{\mathbf{x}}\mathbf{dt} \tag{112}$$

By selecting the right conversion for the matrix $\mathbf{D}$ and using a PI controller of the form

$$\Delta\mathbf{u} = -\mathbf{K_P}\tilde{\mathbf{x}} - \mathbf{K_I}\int \tilde{\mathbf{x}}dt \text{ and } \mathbf{u} = \mathbf{u_{ref}} - \Delta\mathbf{u} \tag{113}$$

and substituting and simplifying the Hamiltonian time derivative (power flow) will result in the **dynamic stability condition** given as

$$\dot{\mathcal{H}} = -\tilde{\mathbf{x}}^T[\mathbf{K_P} - \bar{\mathbf{R}}]\tilde{\mathbf{x}} < \mathbf{0} \tag{114}$$

The performance is determined by the selection of the proportional controller diagonal gain matrix, defined as positive definite.

The nonlinear HSSPFC design is composed of both feedforward and feedback portions. The feedback controller design integrates the energy storage into the AC bus grid. It includes both the feedback into the guidance command algorithm for the boost converter duty cycles and implements the energy storage systems. The duty cycle servo control is fully coupled and the HSSPFC for the energy storage is decoupled due to the skew-symmetric form of the R matrix. This HSSPFC design is primarily for the dynamic transient development.

3.7.4 Example 2: Kundur "like" Model

A Kundur like model was assembled representing four separate grid systems and two load busses. This reduced order model follows the previous development but also includes a spinning machine representation. This is shown schematically in Figure 42. The preliminary results are shown in Figures 42 to 45 for initial condition offsets for the spinning machines and their corresponding bus voltage response, apparent power, injected currents, and energy storage requirements, respectively. Further investigations are warranted with specific details provided for renewable energy generation for each generator model.

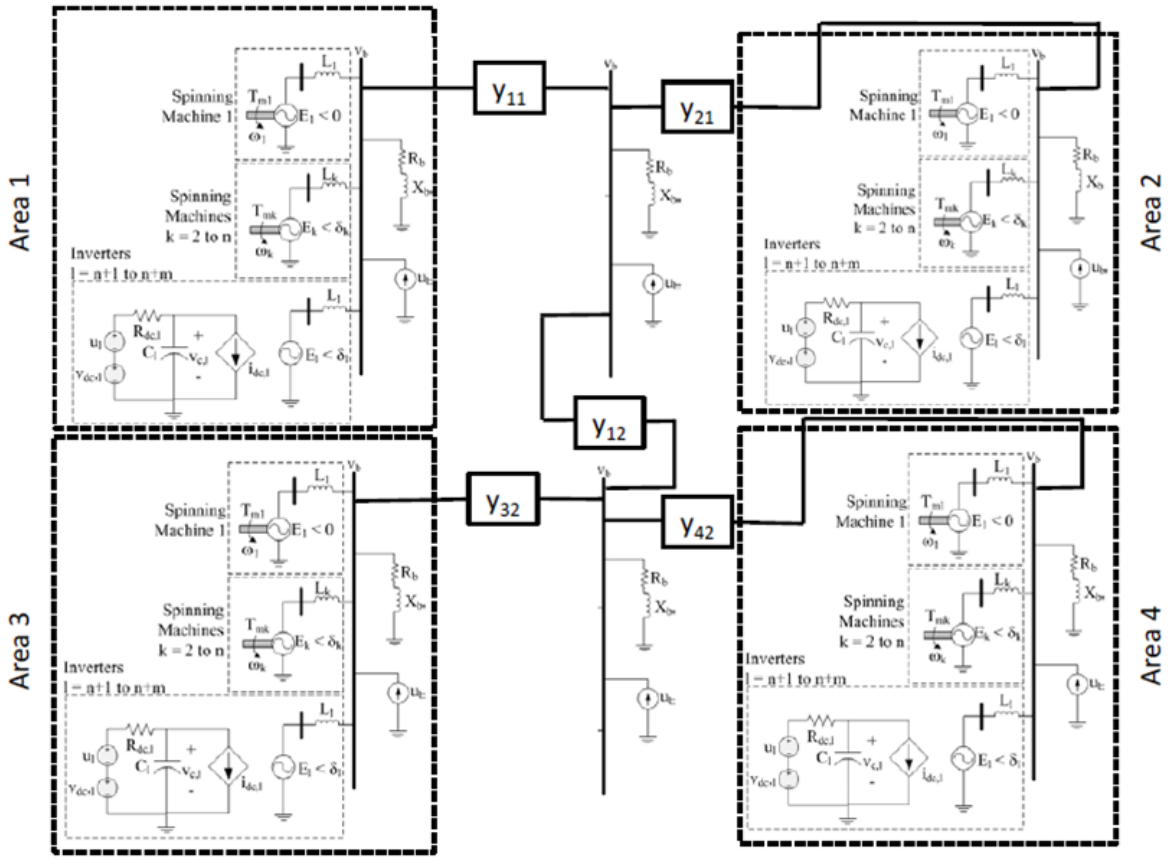

Figure 42: Kundur like model assembled on four separate generators.

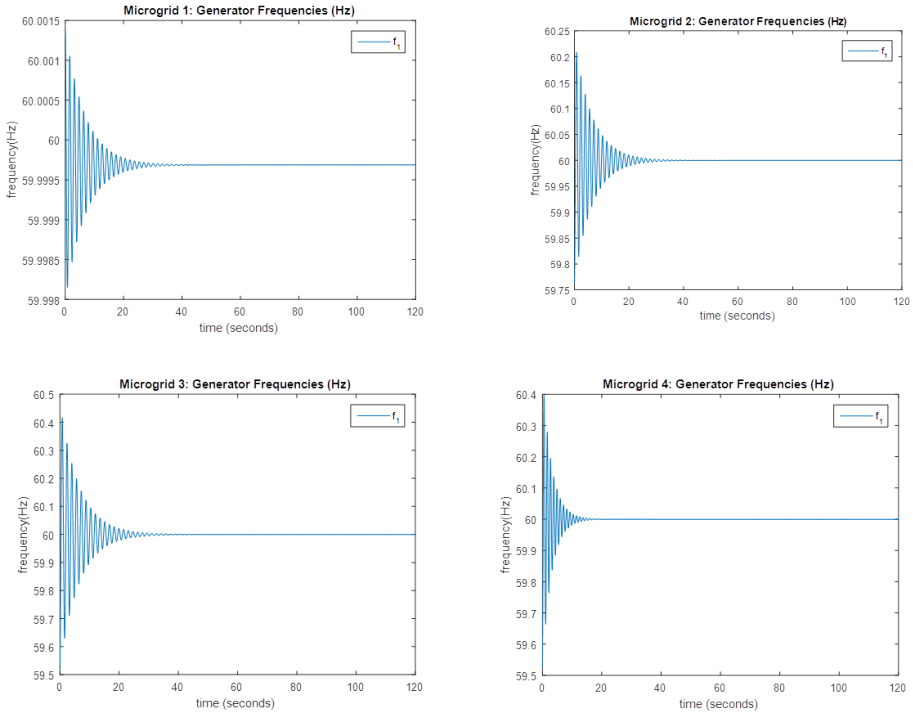

Figure 43: Kundur spinning machine transients four generator system.

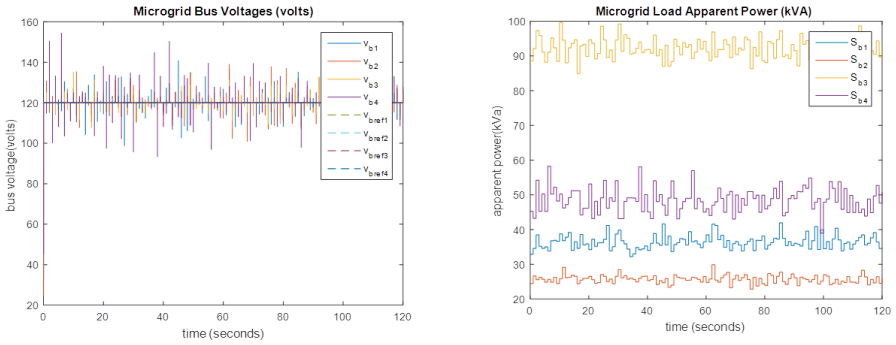

Figure 44: Kundur spinning machine bus voltages (left) and apparent power (right).

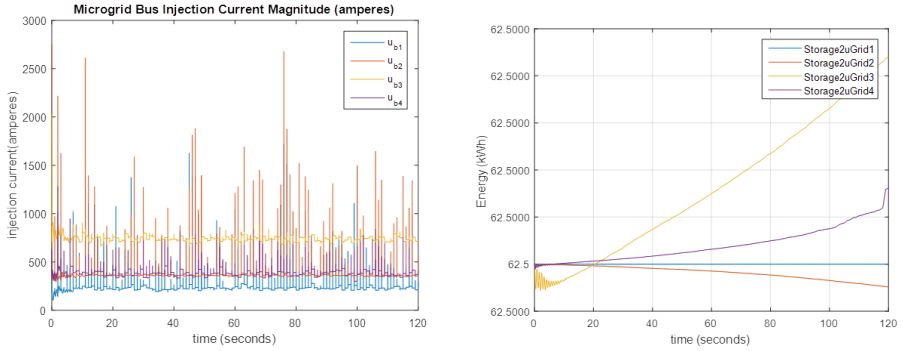

Figure 45: Kundur spinning machine injected currents (left) and energy storage (right).

4 Significant Accomplishments and Conclusions

This one-year effort investigated four potential control design/analysis methodologies for addressing the impact of latency and availability of PV distributed control systems with high penetrations of renewables. The four methodologies considered were: optimal fixed structure control; Nyquist stability; Vector Lyapunov; and Hamiltonian design methods. The most progress was made on the optimal fixed structure control approach. Because of the sheer number of states associated with a power system model, state space methods are typically applied. One drawback of many optimal control design methodologies is the requirement for full state feedback (e.g., access to all system states), or the design of an observer (e.g., Linear Quadratic Gaussian control). In reality, as PMU technology becomes more widespread, there will be an increasing amount of highly accurate data available for control. However, there will likely never be enough PMU's in place in a large power system to measure every state, and if this were to happen, the communication requirements for centralized control would be extreme. Optimal fixed structure control is advantageous because it allows for the design of an optimal controller with limited state feedback, e.g., the state that you can easily observe. This makes it a powerful tool for PMU-enabled grid control schemes. This year we made significant progress developing algorithms and applying this approach to grid control [29]. When full state feedback is available, an optimal control system (e.g., Linear Quadratic Regulator) has inherent robustness: a phase margin greater than 60 degrees and an infinite gain margin (e.g., the controller will be stable for all possible uncertainties in system gain). Currently, no such statement can be derived for optimal fixed structure control. A recommended area for future research is to investigate the potential to guarantee a certain level of performance with limited state feedback. Phase margin is critical for time delay systems because latency directly impacts phase margin.

The Nyquist stability approach was investigated because it elegantly handles time delay and can incorporate performance measures like gain and phase margin. The approach is also readily applied to analytic models as well as system test data (e.g., gain and phase measurements as frequency is swept). We developed numerical techniques for applying this method to large power systems, and were able to successfully identify stable gain regions with guaranteed levels of performance (e.g., gain and phase margin) for different levels of time delay using the minni-WECC model. Since the algorithm requires testing every potential system transfer function, the algorithm has difficulty scaling to large power systems. If the assumption can be made that all controller gain values are the same, the algorithm can be applied to moderately large models. There is some precedent for this type of assumption, for example, a gain of 5% is typically employed for frequency droop. If this assumption can't be made, the approach quickly becomes too computationally expensive. The number of ESAC criterion tests that must be performed, N, is given by

$$N = n^2 \times fpts \times Kpts^{NC} \times Tpts \tag{115}$$

where n is the size of the A matrix, $fpts$ is the number of frequency points, $Kpts$ is the number of gain values tested, $Tpts$ is the number of time delay values of interest, and NC is the number of control systems with independent gain settings. For minni-WECC system with 34 generators, a test of 10 possible gain values results in 10^{34} potential cases without accounting for the number of states, frequency points, and time delay values. One promising application that would not suffer from this limitation is wide area control based on PMU data where the number of PMU's and actuators is limited, and where one is mostly concerned with the robustness of the controller and the stability of the overall system can be verified by other means.

The vector Lyapunov approach was selected because it is well suited to analyze the stability of distributed control systems with structured perturbations. The structured perturbations may be used to model a combination of plant uncertainty and communications uncertainty (e.g., guarantee stability with

or without a particular communications link). This approach is well suited to state space systems, and easily handles nonlinear systems. Results were obtained for several simple test cases with a two-area system. Two difficulties with the application of this control approach were identified. First, the most straightforward approach assigns an uncertainty of $\epsilon \in [0, 1]$ for the interconnection stiffness between different areas. While this parameter can change, and will go to 0 if the line is opened, it limits the range of acceptable stable controllers because it is likely too conservative of a requirement. This can be remedied by expanding the state space and bringing in states from other areas into each subsystem. The second difficulty is associated with automatically partitioning a large state space model into a decomposition of distributed systems. An approach has been proposed, the epsilon decomposition [16], but does not address the previous issue of assigning a large uncertainty to the interconnection coefficients. Further research is required to develop algorithms that perform the decomposition and state space expansion/contraction intelligently. This method does not address latency directly, but it can be incorporated via an approximation (e.g., Pade approximation). We still believe that this is a promising technique for handling communications uncertainty.

The Hamiltonian Surface Shaping and Power Flow Control (HSSPFC) design methodology was selected to investigate grid systems for energy storage requirements to support high penetration of variable or stochastic generation (such as wind and PV) and loads. Specially designed models that are based on the physical (kinetic and potential) energy of the system (the Hamiltonian) allow for the identification of static stability criterion. The Hamiltonian rate (or power flow) determines the dynamic stability criterion. This lead directly to the stability and performance based on energy storage; power, energy and frequency requirements needed to be realized. The technique allows for the inclusion of nonlinear control law formulations. Several examples were investigated for a OMIB and a four generator Kundur like model. Further developments will need to be explored to expand the technique specific for PV inverter systems operating in coordination with spinning machines.

Finally, some time was spent updating the minni-WECC model with high penetrations of PV, adding solar plant models, and adding linearization code for the solar plant models. We had originally planned to update the model with close to 100% PV generation. This proved more difficult than expected. The input to the optimal fixed structure control and Nyquist approaches is a linearized system model (A, B, C, D). Results were only presented for the nominal (no PV) case because we questioned the validity of the results with PV penetrations (likely a programming bug in the linearization algorithm). The analysis algorithms were developed and demonstrated with the nominal linearization, so once an acceptable linearized model for the minni-WECC is obtained, it is relatively straightforward to run the various solar cases. We were able to get to 75% PV generation without any additional controls, 93% with some minimal controls, and 95% with more focussed voltage support. The difficulty getting to very high penetrations in PV is consistent with difficulties we have seen with PSLF models. Going into the project, we assumed that it would be easier with a reduced order model in Matlab. The development of realistic models of systems with high penetrations of PV should be a priority. To do this properly is a painstaking task. First, one has to make intelligent predictions about the path the grid will take as renewable penetration increases. Then one has to build the new models and get them to run. The farther out in the future one goes (e.g., higher renewable penetrations), the more uncertainty in the models and the associated predictions. There are components that can probably be addressed with smaller models. For example, the performance of phase-locked-loops in inverters as grid dynamics become faster is a concern. Ultimately, more time needs to be spent developing suitable grid models for dynamic simulations with very high penetrations of renewables. On a positive note, the eigenvalue and transient response results for increased PV penetrations are consistent with previous PSLF results [11]. Mode frequencies increased with higher renewable penetrations and there was minimal impact on mode damping.

5 Inventions, Patents, Publications, and Other Results

A journal article was published on the application of optimal fixed structure control to the frequency-watt grid support functions for wide area damping of inter-area oscillations in power systems. The citation is listed below:

J. Neely, J. Johnson, R. Byrne, and R. T. Elliott, "Structured optimization for parameter selection of frequency-watt grid support functions for wide-area damping," *International Journal of Distributed Energy Resources and Smart Grids, DERlab/SIRFN Special Issue on Pre-standardization Activities in Grid Integration of DER*, vol. 11, no. 1, pp. 69-94, 2015.

Conference publications have been submitted for the vector Lyapunov and Hamiltonian approaches:

R. H. Byrne, D. J. Trudnowski, J. C. Neely, D. A. Schoenwald, D. G. Wilson, and L. J. Rashkin, "Small Signal Stability Analysis and Distributed Control with Communications Uncertainty," submitted to International Symposium on Power Electronics, Electrical Drives, Automation and Motion, SPEEDAM 2016, June 22-24, Anacapri, Capri Island, Italy.

D. G. Wilson, R. D. Robinett III, W. W. Weaver, and R. H. Byrne, "Nonlinear Power Flow Control Design of High Penetration Renewable Sources for AC Inverter Based Microgrids," submitted to International Symposium on Power Electronics, Electrical Drives, Automation and Motion, SPEEDAM 2016, June 22-24, Anacapri, Capri Island, Italy.

This research continued to foster a relationship between Montana Tech University and Sandia National Laboratories on control of power systems with high penetrations of renewables.

6 Path Forward

While simplified models are excellent for gaining insight into the impacts of increased renewable penetrations, they will not provide an exact answer of what penetration level starts to become problematic (except for the particular simplified model considered). Many of the impacts from increased renewable penetrations are "local problems", as noted in [4, 5]. These can only be identified with accurate system models. Therefore, future distributed control design and analysis tools need to be easily extendable to large power system models. This likely will have to include distribution and sub-transmission models.

The impact of latency, availability, and scalability on the performance of distributed control algorithms for PV generation is a topic that requires significant research to make sure that it does not become a barrier to large-scale adoption of PV generation. This one year effort focussed on latency and availability by looking at four promising control design/analysis methodologies that are appropriate for systems with distributed control, communications latency, and communications uncertainty. Another important topic is cyber security. As more intelligence is integrated into the electric power grid, the associated communications provide more opportunities for an adversary to disrupt larger and larger areas. In addition, the required level of cyber security must not negatively impact the performance or reliability of the power system by inducing an undesirable level of latency. A SunLamp proposal has been submitted to DOE to evaluate the impact of latency, availability, and scalability on grid performance, as well as to evaluate the impact of potential cyber security schemes.

Acknowledgment

This research was sponsored by the U.S. DOE SunShot program under agreement number 29094.

Sandia National Laboratories is a multi-program laboratory managed and operated by Sandia Corporation, a wholly owned subsidiary of Lockheed Martin Corporation, for the U.S. Department of Energy's National Nuclear Security Administration under contract DE-AC04-94AL85000.

References

[1] Disturbance Analysis Working Group of the North American Electric Reliability Council (NERC) Operating Committee, "1996 system disturbances: Review of selected 1996 electric system disturbances in north america," tech. rep., North American Electric Reliability Corporation (NERC), Princeton Forrestal Village, 116-390 Village Boulevard, Princeton, New Jersey 08540-5731, August 2002.

[2] D. J. Trudnowski, D. Kosterev, and J. Undrill, "PDCI damping control analysis for the western north american power system," in *Proceedings of the 2013 IEEE Power and Energy Society General Meeting*, (Vancouver, B.C.), pp. 1–5, July 2013.

[3] E. Grebe, J. Kabouris, S. L. Barba, W. Sattinger, and W. Winter, "Low frequency oscillations in the interconnected system of continental europe," in *2010 IEEE Power and Energy Society (PES) General Meeting*, pp. 1–7, July 2010.

[4] GE Energy, "Western wind and solar integration study," Tech. Rep. NREL/SR-550-47434, National Renewable Energy Laboratory, 1617 Cole Boulevard, Golden, Colorado 80401, May 2010.

[5] N. W. Miller, B. Leonardi, R. D'Aquila, and K. Clark, "Western wind and solar integration study phase 3a: Low levels of synchronous generation," Tech. Rep. NREL/SR-5D00-64822, National Renewable Energy Laboratory, 1617 Cole Boulevard, Golden, Colorado 80401, November 2015.

[6] J. C. Neely, R. Byrne, R. Elliott, C. Silva-Monroy, D. Schoenwald, D. Trudnowski, and M. Donnelly, "Damping of inter-area oscillations using energy storage," in *2013 IEEE Power and Energy Society (PES) General Meeting*, pp. 1–5, July 2013.

[7] R. H. Byrne, D. J. Trudnowski, J. C. Neely, R. T. Elliott, D. A. Schoenwald, and M. K. Donnelly, "Optimal locations for energy storage damping systems in the western north american interconnect," in *2014 IEEE Power and Energy Society (PES) General Meeting*, (Washington, DC), pp. 1–5, July 2014.

[8] C. Silva-Monroy, J. Neely, R. Byrne, R. Elliott, and D. Schoenwald, "Wind generation controls for damping of inter-area oscillations," in *2013 IEEE Power and Energy Society General (PES) Meeting*, pp. 1–5, July 2013.

[9] M. Tabrizi and G. Radman, "PMU-based multi-input SVC supplementary controller for damping inter-area oscillation," in *2010 North American Power Symposium (NAPS)*, pp. 1–6, Sept 2010.

[10] N. Yang, Q. Liu, and J. McCalley, "TCSC controller design for damping interarea oscillations," *IEEE Transactions on Power Systems*, vol. 13, pp. 1304–1310, Nov 1998.

[11] R. Elliott, R. Byrne, A. Ellis, and L. Grant, "Impact of increased photovoltaic generation on inter-area oscillations in the western north american power system," in *2014 IEEE Power and Energy Society (PES) General Meeting*, pp. 1–5, July 2014.

[12] J. T. Feddema, D. A. Schoenwald, R. D. Robinett, and R. H. Byrne, "Encycloppedia of complexity and science systems," ch. Distributed Controls of Multiple Robotic Systems, An Optimization Approach, Springer Verlag, 2009.

[13] D. D. Siljak, *Decentralized Control of Complex Systems*. Academic Press, 1991.

[14] L. Jocic, M. Ribbens-Pavella, and D. Siljak, "Multimachine power systems: Stability, decomposition, and aggregation," *IEEE Transactions on Automatic Control*, vol. 23, pp. 325–332, Apr 1978.

[15] J. Willems, "Direct method for transient stability studies in power system analysis," *IEEE Transactions on Automatic Control*, vol. 16, pp. 332–341, Aug 1971.

[16] A. I. Zecevic and D. D. Siljak, "Parallel solutions of large riccati equations using epsilon decomposition," in *Proceedings of the* 37^{th} *IEEE Conference on Decision and Control*, vol. 6, pp. 4428–4433, December 1998.

[17] J. Wolfe and D. Chichka, "An efficient design algorithm for optimal fixed structure control," in *Proceedings of the* 36^{th} *IEEE Conference on Decision and Control*, vol. 3, pp. 2625–2627, Dec 1997.

[18] C. Abdallah, P. Dorato, J. Benites-Read, and R. Byrne, "Delayed positive feedback can stabilize oscillatory systems," in *1993 American Control Conference*, June 1993.

[19] R. D. Robinett and D. G. Wilson, *Nonlinear Power Flow Control Design: Utilizing Exergy, Entropy, Static and Dynamic Stability, and Lyapunov Analysis*. London: Springer-Verlag London Ltd., 2011.

[20] W. Yang, F. Yang, and J. Chen, "Distributed predictive control of grid-connected solar pv generation based on data-driven subspace approach," in *2014 International Electronics and Application Conference and Exposition (PEAC)*, pp. 1087–1092, Nov 2014.

[21] W. Qi, J. Liu, and P. Christofides, "Distributed supervisory predictive control of distributed wind and solar energy systems," *IEEE Transactions on Control Systems Technology*, vol. 21, pp. 504–512, March 2013.

[22] Y. Jia and X. Liu, "Distributed model predictive control of wind and solar generation system," in *2014* 33^{rd} *Chinese Control Conference (CCC)*, pp. 7795–7799, July 2014.

[23] Z. Nagy and F. Allgower, "Nonlinear model predictive control: From chemical industry to microelectronics," in 43^{rd} *IEEE Conference on Decision and Control, 2004 CDC*, vol. 4, pp. 4249–4254 Vol.4, Dec 2004.

[24] T. Thi and S. Hara, "Robust model predictive control for discrete uncertain time-varying systems with delay," in *2009 ICCAS-SICE*, pp. 3775–3780, Aug 2009.

[25] J. H. Chow and K. W. Cheung, "A toolbox for power system dynamics and control engineering education and research," *IEEE Transactions on Power Systems*, vol. 7, no. 4, pp. 1559–1564, 1992.

[26] L. Vanfretti, "Power system toolbox webpage." http://www.eps.ee.kth.se/personal/luigiv/pst/Power_System_Toolbox_Webpage/PST.html.

[27] D. Trudnowski and J. Pierre, "Inter-area oscillations in power systems," ch. Signal processing methods for estimating small-signal dynamic properties from measured responses, New York: Springer, 2009.

[28] H. Toivonen and P. M. Mőkilő, "A descent Anderson-Moore algorithm for optimal decentralized control," *Automatica*, vol. 21, no. 6, pp. 743–744, 1985.

[29] J. Neely, J. Johnson, R. Byrne, and R. T. Elliott, "Structured optimization for parameter selection of frequency-watt grid support functions for wide-area damping," *International Journal of Distributed Energy Resources and Smart Grids, DERlab/SIRFN Special Issue on Pre-standardization Activities in Grid Integration of DER*, vol. 11, no. 1, pp. 69–94, 2015.

[30] R. J. Plemmons, "*M-matrix characterizations.I—nonsingular M-matrices,"* Linear Algebra and its Applications*, vol. 18, no. 2, pp. 175–188, 1977.*

[31] P. Kundur, Power System Stability and Control. *New York: McGraw-Hill, Inc., 1993.*

[32] R. D. Robinett III and D. G. Wilson, Nonlinear Power Flow Control Design: Utilizing Exergy, Entropy, Static and Dynamic Stability, and Lyapunov Analysis. *Springer, London, 2011.*

[33] M. Ghandhari, Control Lyapunov Functions: A Control Strategy for Damping of Power Oscillations in Large Power Systems. *Doctoral Dissertation, TRITA-EES-0004, ISSN 1100-1607, Royal Institute of Technology, Stockhom, Sweden, 2000.*

[34] D. G. Wilson and R. D. Robinett III, "Transient stability and performance based on nonlinear power flow control design of renewable energy systems," in IEEE Multi-Conference on Systems and Control*, 2011. Denver, Co., USA.*

[35] D. G. Wilson and R. D. Robinett III, "Transient stability and control of wind turbine generation based on hamiltonian surface shaping and power flow control," in 9th International Workshop on Large-Scale Integration of Wind Power into Power Systems*, 2010. Quebec City, Quebec, Canada.*

[36] T. Hassell, W. Weaver, R. D. Robinett III, D. G. Wilson, and G. G. Parker, "Modeling of inverter based ac microgrids for control development," in IEEE Multi-Conference on Systems and Control*, 2015. Sydney, Australia.*

DISTRIBUTION:

1 Guohui Yuan, Ph.D.
DOE Solar Program SunShot Initiative
U.S. Dept. of Energy
Washington, DC 20585

1 Daniel J. Trudnowksi, Ph.D.
Electrical Engineering Department
Montana Tech University
1300 W. Park Street
Butte, MT 59701

1 MS 0576 Raymond H. Byrne, 5521
1 MS 1033 Shannon Boynton, 10661
1 MS 1033 Abraham Ellis, 6112
1 MS 1104 Charles J. Hanley, 6110
1 MS 1140 Dakota Roberson, 6113
1 MS 1140 David A. Schoenwald, 6113
1 MS 1152 Jason C. Neely, 1353
1 MS 1152 David G. Wilson, 1353
1 MS 1152 Lee J. Rashkin, 1353

1 MS 0899 Technical Library, 9536 (electronic copy)

Sandia National Laboratories